Volume xx (200y), Number z, pp. 1–27

A Survey of Cardiac 4D PC-MRI Data Processing

Benjamin Köhler[1], Silvia Born[2], Roy F. P. van Pelt[3], Anja Hennemuth[4], Uta Preim[5], Bernhard Preim[1]

[1]Department of Simulation and Graphics, Otto-von-Guericke University, Magdeburg, Germany
[2]Division of Surgical Research, University of Zürich, Switzerland
[3]Department of Image Guided Therapy Systems, Philips Healthcare, Best, The Netherlands & Yacht, Eindhoven, The Netherlands
[4]Cardiovascular Research and Development, Fraunhofer MeVis, Bremen, Germany
[5]Department of Diagnostic Radiology, Municipal Hospital, Magdeburg, Germany

ben.koehler@isg.cs.uni-magdeburg.de

Abstract

Cardiac 4D PC-MRI acquisitions have gained increasing clinical interest in recent years. They allow to non-invasively obtain extensive information about patient-specific hemodynamics, and thus have a great potential to improve the diagnosis, prognosis and therapy planning of cardiovascular diseases. A dataset contains time-resolved, three-dimensional blood flow directions and strengths, making comprehensive qualitative and quantitative data analysis possible. Quantitative measures, such as stroke volumes, help to assess the cardiac function and to monitor disease progression. Qualitative analysis allows to investigate abnormal flow characteristics, such as vortices, which are correlated to different pathologies. Processing the data comprises complex image processing methods, as well as flow analysis and visualization. In this work, we mainly focus on the aorta. We provide an overview of data measurement and preprocessing, as well as current visualization and quantification methods. This allows other researchers to quickly catch up with the topic and take on new challenges to further investigate the potential of 4D PC-MRI data.

Categories and Subject Descriptors (according to ACM CCS): I.4.9 [Computing Methodologies]: Image Processing and Computer Vision—Applications J.3 [Computing Applications]: Life and Medical Sciences—

1. Introduction

The visual exploration of blood flow data is a challenging problem that raised considerable interest in the visualization community in recent years [VPBB*10, GNBP11, BPM*13, GLvP*12, KGP*13]. Blood flow may be simulated or measured with quite different processing pipelines. Here, we focus on measured cardiac blood flow. These unsteady vector fields on the complex domain of the human aorta are difficult to visualize effectively, in particular in case of pathologies and the resulting complex flow behavior. In this survey, we discuss not only solutions to the visualization problems, but also the whole pipeline including image acquisition, preprocessing, the extraction of flow features and the quantification of specific measures.

Blood Flow Measurements: Information about blood flow in the heart and its surrounding vessels have been investigated for decades [SW71, PH83], as they can improve the diagnosis and prognosis of *cardiovascular diseases* (CVDs). Earlier advances in *magnetic resonance velocity mapping* [BPFL84, UFK*87] using the *echo rephasing sequence* [PN85, LFN*86, NFL86] are the basis for a *two-dimensional phase-contrast magnetic resonance imaging* (2D PC-MRI) [KFU*87]. Due to its non-invasiveness, decent spatial resolution, and the quantitative character of the data, 2D PC-MRI became a useful tool in the clinical routine to measure regional blood flow in one 2D plane, which is angulated prior to the scan.

The evaluation of 2D PC-MRI data facilitates assessment of, e.g., a heart valve's function by quantifying *flow rates* and determining if there is significant back flow (*regurgitation fraction*) or by evaluating if there is a high *pressure gradient* during the valve's opening phase. The pumped blood per heartbeat (*stroke volume*) is used to evaluate the heart's pumping capacity. Increased *peak flow velocities* and pressure gradients may occur in pathologically narrowed (*stenotic*) vessels. Further quantifiable measures such as *pulse wave velocities* and *wall shear stress* correlate to vessel stiffness and pathologic dilation (*aneurysm*), respectively.

4D PC-MRI: Technical progress in the field of MRI nowadays enables *four-dimensional* (4D) PC-MRI acquisitions (also: *flow-sensitive MRI*, *MR velocity mapping*, *4D flow CMR*). This modality was introduced by Wigström et al. [WSW96] and is able to provide time-resolved, three-dimensional velocity fields. These data allow for an extensive quantitative analysis, since measuring planes can be adjusted *after* the scan – in contrast to 2D PC-MRI, where a new scan is required in case of placement errors or the need of information about further locations.

Another major advantage is that a qualitative analysis of the three-dimensional, pulsatile blood flow becomes possible. Characteristic flow aspects facilitate a deeper understanding of a patient's situation, since specific patterns, such as vortex flow, are correlated to different pathologies. There is, e.g., a high probability of emerging systolic vortex flow in the ascending aorta if the aortic valve is *bicuspid*, i.e., two of the three leaflets are fused [SS07]. This affects the valve's opening characteristics [BHB*13, LBB*14]. Vortex flow close to the vessel wall may induce high shear forces [vOPC*15, GBvO*15] that increase the risk of aneurysm development [BSK*14]. Further understanding this mutual influence of hemodynamics and vessel morphology can support treatment decision-making and the corresponding risk assessment. Advances towards higher resolution and faster acquisitions, as well as studies proving the clinical impact, yielded an increasing interest in 4D PC-MRI in recent years.

Overviews: Hope et al. [HH08, HSD13], Srichai et al. [SLWL09], Ebbers et al. [Ebb11], Markl et al. [MKE11, MSB14], Calkoen et al. [CRvdG*14], Stankovic et al. [SAG*14] and Nayak et al. [NNB*15] provided overviews about 4D PC-MRI and related clinical studies. Sengupta et al. [SPK*12] perform an extensive comparison between phase-encoded MRI, *echocardiographic particle image velocimetry* and *color Doppler echocardiography* for cardiovascular flow visualization. They consider multiple aspects, such as spatio-temporal resolutions, scan time, low- and high-velocity accuracy, and the need for breath-holding. Dyverfeldt and colleagues [DBB*15] – physicists, physicians and biomedical engineers – recently published a 4D PC-MRI consensus paper consisting of shared experiences and ideas. They describe the potential clinical and research utility of 4D PC-MRI flow, as well as achieved and open development goals.

Organization: Section 2 explains 4D PC-MRI acquisitions and related artifacts. Vessel segmentation is described in Section 3. Section 4 characterizes methods to visualize the anatomical context. Qualitative and quantitative data analysis techniques are presented in Section 5 and 6. Section 7 is about the combination of 4D PC-MRI data and CFD for blood flow simulations. Section 8 concludes. This paper is an extension of a previous work [KBvP*15].

2. 4D PC-MR Imaging

A basic understanding of 4D PC - MRI data is essential to develop new analysis methods. Thus, acquisition fundamentals and data characteristics are explained in the following. In this paper, we adopt the common terms 2D PC-MRI and 4D PC-MRI that actually denote time-resolved (*cine*) 2D (2D + time) PC-MRI and *cine* 3D (3D + time) PC-MRI, respectively.

2.1. Physics – Velocity Encoding

Protons in the body have a physical property called *spin*, which can be seen as rotation around an arbitrary, internal axis. Application of the main magnetic field B_0 aligns the protons parallel or antiparallel to the B_0 direction (Figure 1a), where the parallel state has slightly less energy. Consequently, more protons are in this state, yielding an overall magnetization that increases with higher magnetic field strengths. The magnetization in MRI mainly affects hydrogen atoms from water molecules. This allows to distinguish water from fat tissue, but also to encode fluid movement. Typical scanners achieve 1.5 or 3 T, newer models even 7 T. For comparison, the earth's magnetic field strength is about 3.2×10^{-5} T at 0° latitude and 0° longitude. The protons, however, are not fully aligned with the B_0 direction; they *precess* like gyroscopes. The individual precessions are out of *phase* (unaligned).

For flow measurements, a linear magnetic field gradient is applied that causes a phase shift depending on an atom's position (Figure 1b). The application of the inverted gradient erases this effect in static tissue (*bipolar gradients*). In the moving blood, however, there is a measurable phase differ-

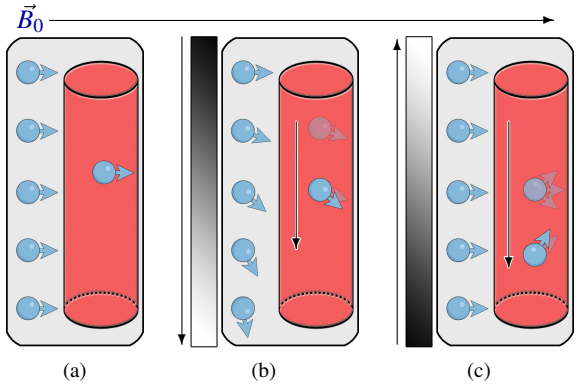

Figure 1: (a) The B_0 magnetic field aligns all **protons** (**blue**) in **stationary tissue** (**gray**) as well as **vessels** (**red**). (b) A magnetic gradient field causes a position-dependent phase shift. (c) The inverted gradient removes the phase shifts in stationary tissue. Phase encodes the velocity in moving fluids. Images based on Lotz et al. [LMLG02].

ence, since the atom receives different parts of the gradient. This difference is directly related to the flow velocity (Figure 1c).

Datasets: Three *phase* (also: *gradient*, *velocity*) images $V_{\{x,y,z\}}$ are reconstructed by calculating all phase differences. Each image contains the velocity values in one of the spatial directions x, y and z. From these three components, a 3D velocity vector field V is reconstructed, which forms the basis of all further flow analyses. Another reconstruction process yields undirected flow strengths into three *magnitude* images $M_{\{x,y,z\}}$. These data are less error-prone to uncorrelated noise (Figure 2c). In an analogous manner, one combined magnitude image M is generated. However, this is not suitable for the calculation of quantitative measures. An anatomy image A is derived from averaging signal intensities (Figure 2b). Some papers refer to this as magnitude image instead.

A dataset contains a full heartbeat, which is the average of multiple cardiac cycles during several minutes. Typical resolutions are 1.5–2.5 mm between data points in a slice, with slice distances of 2–4 mm and 20–50 ms between subsequent time steps, often abbreviated as, e.g., $2 \times 2 \times 3.5$ mm/40 ms. This yields a grid with about 150×200 voxels in each of the 20–50 slices and 15–40 temporal positions. The data are usually stored in a 12 bit unsigned integer, with values ranging from 0 to 4095, where 2048 corresponds to zero velocity, and values below and above 2048 correspond to negative and positive velocities along the current spatial dimension, respectively.

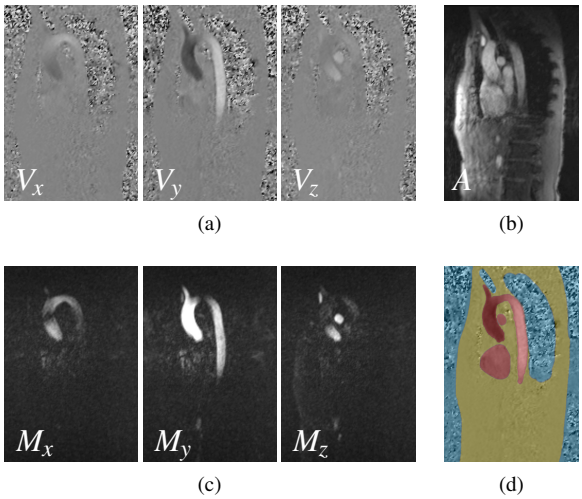

(a) (b) (c) (d)

Figure 2: Thoracal images of the aorta (seen from the side) at a specific time point during the heart cycle. Phase $V_{\{x,y,z\}}$ (a), anatomy A (b) and magnitude images $M_{\{x,y,z\}}$ (c). (d) Labeling of the **thoracic aorta and heart** (**red**), **body** (**yellow**) and **air** (**blue**).

Scan Parameters: The two bipolar magnetic field gradients are adjusted so that the maximum phase shifts of $\pm 180°$ correspond to the *velocity encoding* (V_{ENC}). This essential scan parameter describes the maximum measurable blood flow velocity between $\pm V_{ENC}$ [m/s] per dimension. Exploiting the full range by setting the V_{ENC} to the highest expected velocity is desired to obtain higher phase differences, resulting in increased image contrast and quantitative precision. A common choice for aortic blood flow is $V_{ENC} = 1.5$ m/s [Mar05, MFK*12]. Flow velocities in the ventricles or pathologically narrowed vessels may differ greatly from this value. Thus, adjusting the scan to the blood flow in a specific region is crucial. Buonocore [Buo93] used a modified MR sequence that allows the usage of two V_{ENC} values. He used 2 and 0.3 m/s during systole and diastole, respectively, leading to significantly improved ascending aortic flow measurements. However, this has not been used for clinical routine so far [LMLG02]. Nett et al. [NJF*12] also described a dual V_{ENC} approach. They combined flow images with different V_{ENC} to cover a wide range of velocities (high V_{ENC}) and still obtain a decent contrast (low V_{ENC}). However, acquisition times increase and an image composition scheme is required.

Acceleration Techniques: Acquisition times are a crucial factor for the applicability of 4D PC-MRI in the clinical routine. Advances in recent years reduced scan times from more than 30 min to about 8–12 min for the aorta and 10–20 min for the whole heart [SAG*14]. Nayak et al. [NNB*15] provided an overview of corresponding techniques such as the *broad-use linear speed-up technique* (k-t BLAST) [TBW01], *sensitive encoding* (k-t SENSE) [PWSB99] and *generalized autocalibrating partially parallel acquisitions* (k-t GRAPPA) [GJH*02]. Schnell et al. [SME*14] reduced scan times by 28% to 68% using k-t GRAPPA. Hess et al. [HBN*15] demonstrated an increased signal-to-noise ratio (SNR) at 7 T field strength, compared to flow acquisitions using 1.5 T and 3 T, which can be utilized to accelerate the scans or improve image resolutions.

Repeatability: Wentland et al. [WGW13] found a strong repeatability of 4D PC-MRI measurements in a study with ten healthy volunteers where each individual was scanned twice. Van Ooij et al. [vOPP*15] confirmed the reproducibility of systolic flow velocities and wall shear stress in healthy volunteers.

2.2. Artifact Correction

Bakker et al. [BHV99] described general sources of errors in 2D PC-MRI flow measurements that also occur in its 4D counterpart. Among others, this comprises *partial volume effects*, *phase wraps* (also: *aliasing*) and *velocity offsets* due to various causes. Many artifacts can be corrected in a post-processing step. This is necessary to increase the precision of quantitative results and the quality of flow visualizations.

2.2.1. Phase Unwrapping

If the blood flow velocity exceeds the V_{ENC}, it appears as a flipped value in the image data, which means that the measured flow seemingly runs in the opposite direction. Assuming that velocities of spatio-temporally adjacent voxels should not differ by more than V_{ENC}, such *phase wraps* can be identified and corrected [BKHM07] (Figures 3a–3c). Phase wraps may occur in various MRI-based measurements. We follow a classification of phase unwrapping methods by Loecher et al. [LSJW15]. A weakness that all of the mentioned methods share is that they are not capable of correcting multiple phase wraps, which means that a pixel is wrapped at least twice.

Methods for MRI: General phase unwrapping methods are not specifically tailored towards the phase-contrast MRI context. Cusack et al. [CP02] described a robust, iterative 3D phase unwrapping that estimates the noise per voxel and processes voxels with low noise first. The unwrapping is performed in adjacent voxels of a specified seed point and a manually initialized noise threshold is gradually increased in each iteration. Jenkinson [Jen03] described a fully automatic method suitable for n-dimensional images that is based on a *greedy cost-function optimization*. It takes about 20 min for larger 3D datasets and might scale unacceptably for 4D PC-MRI data. Bioucas-Dias et al. [BDV07] utilized *graph cuts* to perform an energy minimization based on first-order *Markov random fields*. The method was applied solely to artificial data.

Methods for PC-MRI: Other methods were specifically designed for PC-MRI data. They often exploit spatial continuity and phase singularity [BWK97, AHGB09]. Song et al. [SNPG95] assume that phase changes between pixels are less than V_{ENC}. A least-squares problem is formulated of which the solution equals the solution of a Poisson equation, allowing the usage of fast Poisson solvers. Though, the success of their algorithm strongly depends on an incorporated sequence of thresholds.

Methods for cine PC-MRI: Methods for time-resolved PC-MRI data often consider temporal continuity. Xiang [Xia95] calculated *differential velocity maps* (DVMs), which were shown to be free of aliasing artifacts, between adjacent time steps and a *reference velocity map* as integration of the DVMs. Both are combined in a 1D *temporal phase unwrapping*. Yang et al. [YBK*96] used the anatomy image A to estimate the pixelwise motion between subsequent time steps, which ensures that unwrapped pixels represent the same flow region. Salfity et al. [SHG*06] compared the performance of phase unwrapping algorithms that consider one, three and four dimensions. Loecher et al. [LJLW11] use a probabilistic measure in a 4D gradient-based approach to decide if a voxel is phase wrapped. Untenberger et al. [UHT*15] employed spatial and temporal constraints by using a region of interest (ROI) and by demanding temporal continuity in forward and backward direction, respectively.

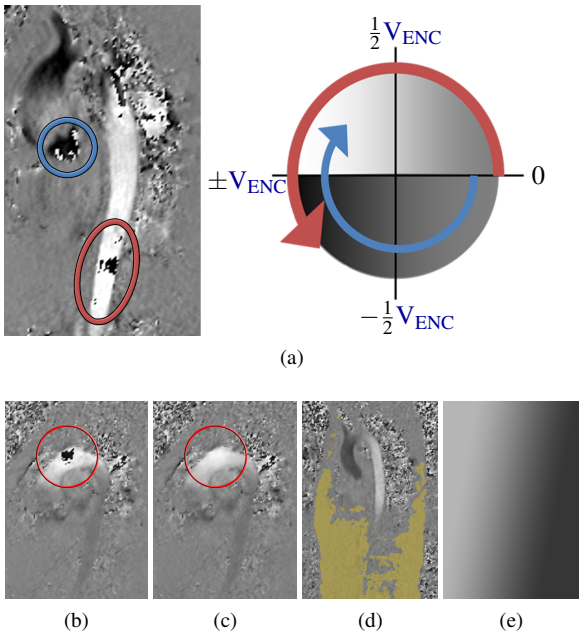

Figure 3: (a) Phase unwrapping. The wrapped velocities are $\frac{3}{4} \cdot V_{ENC}$ (**blue**) and $-\frac{3}{4} \cdot V_{ENC}$ (**red**). The corrected velocities are $\frac{5}{4} \cdot V_{ENC}$ of opposite sign. (b–c) Phase image **before and after** (**red**) phase unwrapping. (d–e) Estimated **static tissue mask** (**yellow**) and fitted 2D gradient as phase offset approximation.

Schofield et al. [SZ03] described a method based on *Laplacian operators*, which has been shown to be useful for MRI [VZ03, BEJE08, LAW*14]. Loecher et al. [LSJW15] combined spatio-temporal continuity in all four dimensions with the Laplacian-based approach and proposed a fully automatic, single-step method.

2.2.2. Velocity Offset Correction

Measurement errors can cause a shift (an *offset*) of the true flow velocities. There are three major causes [LBS*14]:

1. *Eddy currents* [WCS*93, CSCW07] in the magnetic field are caused by rapidly switching the velocity encoding gradients.
2. *Concominant gradient* (also: *Maxwell*) *terms* [BZP*98] are related to terms of the Maxwell equation for the curl and divergence of a magnetic field. A nonlinear, spatially dependent magnetic field, which produces phase errors, is always generated.
3. *Gradient field nonlinearity* [MBA*03, PBB05] denotes that the magnetic field coils are not able to produce a perfectly accurate field. Thus, there is always an inhomogeneous distribution.

Cause 2 and 3 can be corrected during the image reconstruction without user interaction [SAG*14]. Bernstein et al.

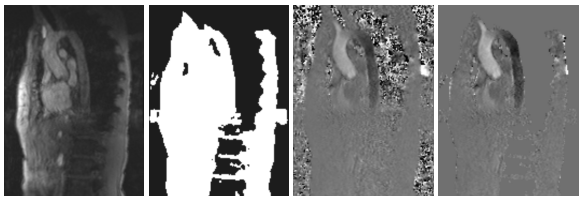

(a) (b) (c) (d)

Figure 4: (a) Anatomical image A. (b) User-adjusted threshold on A. Original (c) and masked (d) flow image V. One slice and temporal position of V_y is shown as an example.

[BZP*98] proposed modifications to the phase contrast pulse sequence and an adapted reconstruction method to minimize the effects of Cause 2. Markl et al. [MBA*03] showed that measurement errors due to Cause 3 are directly related to model-based predictions, which can be used to correct the gradient field distortion, and presented a corresponding generalized reconstruction.

Eddy current correction: However, an *eddy current* (also: *velocity offset*, *phase offset*) *correction* is required during the data processing. This systematic, non-constant error, which affects both the stationary tissue and the vessels, can be subtracted from the image. For this purpose, Walker et al. [WCS*93] calculated the standard deviation σ for each voxel in the phase image along the temporal dimension. The temporal σ is highest for air and lowest for static tissue. Vessels are in between. Based on the assumption that obtained flow velocities in static tissue are erroneous, an approximate static tissue mask (Figure 3d) is created via interactive thresholding on the temporal σ image. One plane per phase image slice per temporal position is fitted to the velocity values of the static tissue mask (Figure 3e) and then subtracted from the corresponding phase image slice. Bock et al. [BKHM07, Boc12] suggested to fit only one plane to slices from the late diastole, since here the aorta and pulmonary artery have the least motion, and use this for the correction of all time steps. Lankhaar et al. [LHM*05] and Chernobelsky et al. [CSCW07] showed that such corrections improve quantification results. Fair et al. [FGG*13] investigated improvements when using data with a higher signal-to-noise ratio. Lotz et al. [LMLG02] pointed out that phase offset corrections can also introduce new errors and have to be applied carefully. They instead process only the local surroundings of the target vessel. Lorenz et al. [LBS*14] underlined the importance of velocity offset corrections to substantially improve flow visualizations.

2.2.3. Noise Masking

Bock et al. [Boc12] proposed a masking of noisy flow values in the phase images, mostly present in the lungs or in the surroundings of the patient. Their removal can be important to enhance the quality of anatomical context rendering (Section 4.2) or to improve particle system-based flow visualizations (Section 5.2.2) by diminishing random movements if a particle leaves the vessel. To select air-filled regions, they performed a thresholding on either the anatomical image A or on the temporal σ image proposed by Walker et al. [WCS*93]. The threshold is either set interactively or using a heuristic, e.g., that the values' top 15% represent air in the temporal σ image or bottom 15% in A. The resulting binary mask (Figure 4b) is then multiplied with the flow image V (Figures 4c–4d). For this purpose, the velocity values in each phase image $V_{\{x,y,z\}}$ should be scaled to $[-V_{ENC}, +V_{ENC}]$ so that zero means no flow. However, a careful application is recommended since parts of the vessel and intravascular flow can be removed.

2.2.4. Divergence Filtering and Regularization

Blood, as an incompressible fluid, should be divergence-free, which might not be the case in the acquired data due to measurement errors. *Divergence filters* suppress these divergent components. Tafti et al. [TDGSU11, TU11] proposed a variational reconstruction method, which employs total-variation regularization, while incorporating flow curl and divergence. Loecher et al. [LKTW12] described positive effects of divergence-free filters on the integration of streamlines. They evaluated connectivity by counting streamlines, which were seeded on an emitter plane, that reach another plane inside the vessel before leaving the vessel due to flow field inaccuracies. Bostan et al. [BVP*13] additionally incorporated conditions about the flow's rotational behavior

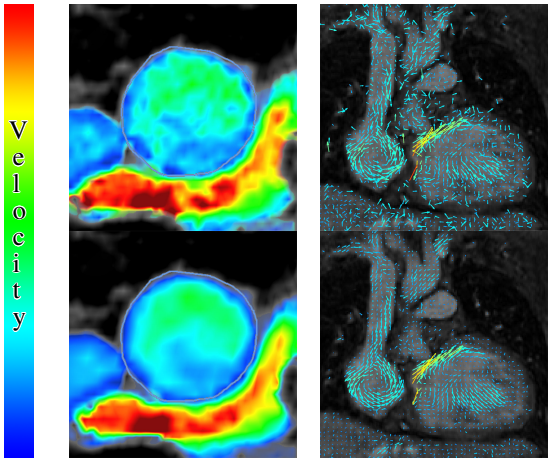

(a) (b)

Figure 5: Flow profile in the ascending aorta's cross-section (a) and flow vectors $\vec{v}$ of one slice through the heart (b) before (top) and after (bottom) divergence filtering [OUT*15]. Images provided by F. Ong.

and assumed that flow varies smoothly over time. They introduced a flow field regularization that improved the visualization of helical patterns in 4D PC-MRI data of the aorta. However, a quantitative comparison was not performed. Thus, it is not clear if the calculation of quantitative measures remains reliable. For the calculation of pressure differences from measured 4D flow, divergence filtering did not change the results significantly [MHD*13]. Later, Bostan et al. [BLV*15] described a regularization based on the nuclear norm, which is the sum of singular values, of the flow field's Jacobian matrix J. A better SNR performance was shown for phantom data and an improved streamline visualization was established for 4D PC-MRI data. Santelli et al. [SLB*15] penalized divergence in flow fields measured with undersampled 4D PC-MRI using divergence-free wavelets or a finite difference method based on the ℓ_1-norm of divergence and curl. Ong et al. [OUT*15] described a technique based on a wavelet transform that is robust to segmentation errors and improves visualization, while preserving quantification results (Figure 5).

3. Vessel Segmentation

For many analysis and visualization tasks, a vessel segmentation or approximation is required. There are various 3D vessel segmentation techniques for angiography data from MRI or CT. Therefore, one approach is to generate an image similar to MR angiography from the 4D PC-MRI data and then use well-established algorithms. Lesage et al. [LABFL09] provided a corresponding overview of methods that are not tailored to cardiac vessels. Mirzaee et al. [MH15] fused flow images with additional anatomical data to improve the segmentation of, e.g., stenotic vessels. In this section, we explain selected approaches that solely use 4D PC-MRI image data.

3.1. PC-MRI-based Angiographies

An automatic 4D segmentation is challenging, since image contrast depends on the time-varying blood flow velocities that are typically lower during diastole. Manual 4D segmentation of the whole vessel is not feasible in clinical practice due to the enormous expenditure of time. A common approach is to derive a 3D contrast-enhanced image, which resembles MR angiography, but no longer has temporal information.

TMIP: A *temporal maximum intensity projection* (TMIP) obtains the maximum velocity per voxel along the temporal dimension of size T. Usually, this technique is applied to the magnitude image M [VPBB*10]:

$$\mathbf{TMIP}(\vec{p}) = \max_t \left(||\mathrm{M}(\vec{p}_t)|| \right) \tag{1}$$

The TMIP is bright at positions $\vec{p} \in \mathbb{R}^3$, where fast blood flow was present at some time $t = 0 \ldots T-1$ during the cardiac cycle (Figure 6a). Inflow jets may appear prominently. Distant vessel sections can lose contrast due to decreasing velocities. Further contrast variations might be caused by the typically parabolic flow profile, which means that the highest velocities are located in the center. This profile can be disturbed in case of vortex flow.

PCMRA: A *phase-contrast magnetic resonance angiography* (PCMRA) image [HFS*11] combines the anatomy image A with the phase image V. Both have a high vessel contrast, but an opposing high and low contrast for static tissue and noise regions. The PCMRA can be calculated using:

$$\mathbf{PCMRA}(\vec{p}) = \sqrt{\frac{1}{T} \cdot \sum_{t=0}^{T-1} \mathrm{A}^2(\vec{p}_t) \cdot ||\mathrm{V}(\vec{p}_t)||^2} \tag{2}$$

or similar formulae [BWJ*08]. A temporal average instead of the maximum is calculated (Figure 6b).

LPC: Chung et al. [CNS04] defined *local phase coherence* (LPC) (Figure 6c) as the average angle between a normalized velocity vector and its normalized neighbors at $\vec{p}_t{}^n$:

$$\mathbf{LPC}(\vec{p}_t) = \frac{1}{26} \cdot \sum_{\forall \vec{p}_t{}^n} \frac{\mathrm{V}(\vec{p}_t) \cdot \mathrm{V}(\vec{p}_t{}^n)}{||\mathrm{V}(\vec{p}_t)|| \cdot ||\mathrm{V}(\vec{p}_t{}^n)||} \tag{3}$$

The normalization causes insensitivity towards the actual velocities, which might be advantageous in vessels with slower blood flow or if the image contrast is poor due to a $\mathrm{V_{ENC}}$ chosen too high.

EVC: Similar to the LPC, Solem et al. [SPH04] described *eigenvalue coherence* (EVC) (Figure 6d), which is based on an eigenvalue analysis of a local velocity tensor:

$$\mathbf{EVC}(\vec{p}_t) = \frac{4 \cdot \lambda_0 \cdot \lambda_1}{(\lambda_0 + \lambda_1)^2} \quad \text{with} \tag{4}$$

$$\{\lambda_0 \geq \lambda_1 \geq \lambda_2\} = \mathrm{eig}\left(\frac{1}{26} \cdot \sum_{\forall \vec{p}_t{}^n} \mathrm{V}(\vec{p}_t) \cdot \mathrm{V}(\vec{p}_t)^{\mathrm{T}} \right)$$

LPC and EVC both preserve temporal information, which

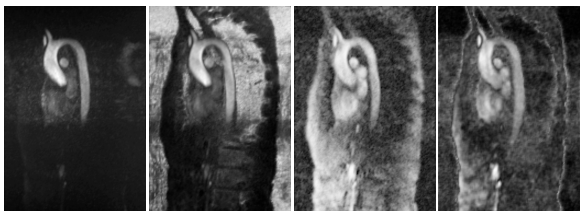

(a) TMIP (b) PCMRA (c) LPC (d) EVC

Figure 6: 3D images with enhanced vessel contrast. (a) Temporal maximum intensity projection of the magnitude image M. (b) Phase-contrast magnetic resonance angiography image. Time-averaged local phase (c) and eigenvalue coherence (d).

enables the subsequent application of either temporal averaging, as the PCMRA does (Equation 2), or a TMIP (Equation 1), where M is substituted accordingly. Temporal averaging produces better results, since the LPC and EVC images tend to be noisy.

3.2. Lumen Segmentation - 3D

A 3D vessel mask is an approximation of the dynamic vessel morphology and can be used for the subsequent anatomical context visualization, for quantification purposes or for the extraction of a centerline. Tagliasacchi [Tag14] provided an overview of centerline extraction methods. The *Vascular Modeling Toolkit* (VMTK) [PVS*09] provides corresponding functionality specifically for vascular structures [AIR03].

Region-based Approaches: Hennemuth et al. [HFS*11] used a *watershed transformation* on a PCMRA image, where the user specifies include and exclude points. Stalder et al. [SGGJ13] clustered the temporal σ image [WCS*93] (Section 2.2.2) into air, static tissue and vessels. The method is fully automatic, but does not allow to distinguish between different vessels.

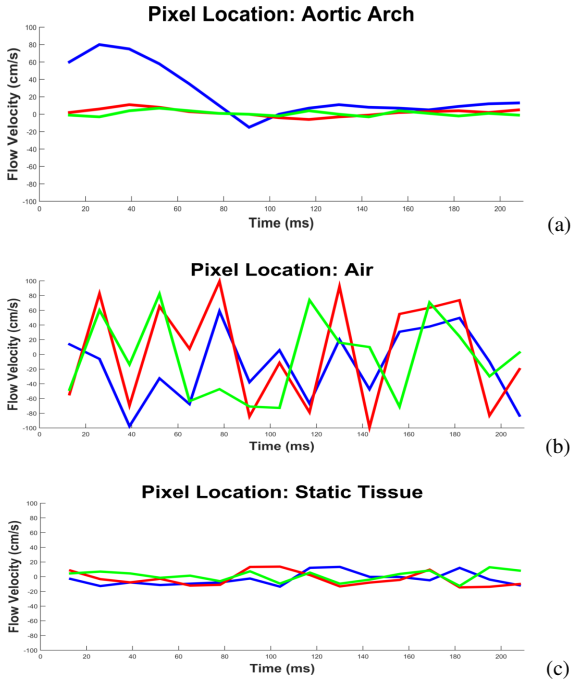

Figure 7: Time-dependent flow curves for each of the three spatial dimensions (**red**, **green**, **blue**) for a pixel inside the aortic arch (a), air (b) and static tissue (c). The **blue curve** in (a) resembles a typical healthy volunteer's flow curve and is to be identified by a curve fitting procedure. Images based on Bergen et al. [BLAB15].

Graph-based Approaches: Köhler et al. [KPG*15c] used *graph cuts* [BK04,LS10,JSH12] on the TMIP, where regions inside and outside the vessel are user-provided via drawing. Gülsün et al. [GT10] computed a centerline based on a *medialness map* between user-specified seeds on a PCMRA image and extracted the vessel lumen using a graph cut with the centerline as input.

Model-based Approaches: Van Pelt et al. [VPNtHRV12] used an *active surface model* on the TMIP, where three parameters for internal and external forces of the energy minimization can be adjusted. Volonghi et al. [VTC*15] estimated the vessel via thresholding on a PCMRA image, which was filtered with anisotropic diffusion. An initial surface is extracted using marching cubes and a corresponding centerline is approximated. This is used as initialization for an automatic *level set* segmentation. Bergen et al. [BLAB15] analyzed each voxel in $V_{\{x,y,z\}}$ along the temporal dimension. When plotted, one curve should resemble a typical flow curve, whereas outside voxels produce noise curves (Figure 7). A GPU-based curve fitting is performed to find the mean and standard deviation of the assumed normal distribution. Subsequent interval thresholding generates an approximative segmentation that is used as input for a *geodesic active contour* (GAC) on the temporal position of the anatomy image A, where the contrast is highest (typically during peak-systole).

3.3. Lumen Segmentation - 4D

A 4D vessel segmentation facilitates the depiction of the vessel movement. It can be employed for quantification with increased accuracy and is crucial to calculate measures such as wall shear stress that interact with the vessel wall.

Graph-based Approaches: Köhler et al. [KPG*15b] described a procedure to automatically segment the aorta in each temporal position. The user performs an initial 3D graph cut-based segmentation (Section 3.2) on a TMIP image as basis. The resulting mesh, which is extracted via marching cubes, represents the maximum vessel extent. Based on the assumption that the vessel diameter does not shrink more than 50% during diastole, the 3D graph cut is automatically set up for each time step of the anatomy image A. Intravascular regions are initialized using a dilated centerline, regions outside with a dilated contour of the mesh.

Model-based Approaches: Bustamante et al. [BPE*15] created an *atlas* from the dataset of a healthy volunteer, which was segmented on a PCMRA image and contains multiple vessels as well as standardized measuring planes. The atlas was used to obtain time-resolved segmentations of other datasets using robust *affine registrations* as initialization, followed by *non-rigid registrations* as fine-tuning. The net flow volume (Section 6.1.1) was automatically obtained for each defined measuring plane. Their method requires datasets that were scanned with an equal orientation. Thus,

a possible application is the evaluation of studies. However, pathologic cases with vessel morphologies that strongly differ from the atlas, are problematic.

3.4. Cross-section Segmentation

Quantification methods often require an *accurate* definition of the lumen in a measuring plane orthogonal to the vessel. Obtaining this from a 3D segmentation without temporal information might introduce errors, since the vessel pulsation is neglected. Also, in contrast to the voxels of the 3D segmentation, measuring planes are not necessarily parallel to the image axes. Consequently, 2D cross-section segmentations that are sampled from a 3D lumen segmentation might have a square-edged boundary. Instead, manual contour drawing can be carried out by the user. However, this might be tedious if multiple evaluations are performed or if time-resolved cross-section segmentations are required. The problem is well-known from the 2D PC-MRI context. There, many tools let the user create one contour that is then automatically propagated over time and readjusted in each temporal position based on the image intensity gradients (edges).

Region-based Approaches: Van Pelt et al. [VPBB*10] detected cross-sections in the TMIP based on an *eigen-decomposition* of a local structure tensor for user-given query positions. The results were used as seeding planes for the subsequent blood flow visualization.

Model-based Approaches: Goel et al. [GMK*14] described an automatic method to find vessel cross-sections in the anatomy image. They perform an edge detection on 2D image slices and use a *Hough transform* to determine the most circular objects in each temporal position.

4. Anatomical Context Visualization

When the complete intravascular flow is shown, one gets a good impression of the vessel shape (Figure 8c). However, this might not be the case when exclusively specific flow features, such as vortices, are shown. Here, the vessel anatomy can be displayed as orientation and contextual information. Vessels are either extracted from 3D lumen segmentations (Section 3.2) or depicted via direct volume rendering of a 3D high contrast image (Section 3.1). Both approaches are outlined in the following. In addition, we briefly describe approaches to extract and visualize time-varying surface meshes.

4.1. Geometric Surface Meshes

If different vascular structures have separate meshes, single vessels can easily be hidden to focus the evaluation or reduce visual clutter.

Static Vessels: To extract triangular surface meshes from

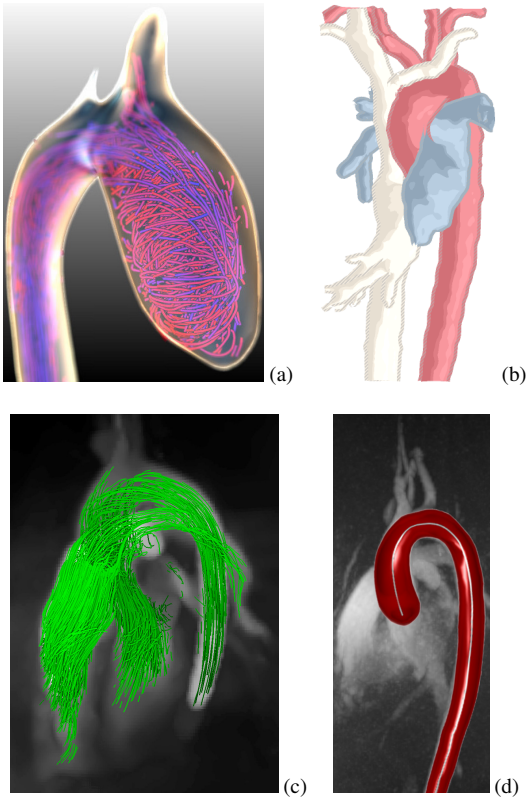

Figure 8: Anatomy visualization with surface meshes (a–b) and direct volume rendering (DVR), more precisely, maximum intensity projection (c–d). (a) A ghosted viewing of the culled vessel front emphasizes the shape perception. Image provided by K. Lawonn. (b) Cel shading. Image provided by B. Behrendt. (c) Flow provides an impression of the vessel shape. (d) Combined geometric surface and DVR.

3D segmentations, *marching cubes* [LC87] or *constrained elastic surface nets* [Gib98] can be employed . Mesh-based rendering techniques can be applied to create appealing visualizations. A common way to make intravascular flow visible is to render only the vessel's back side, as seen from the viewer's position. Gasteiger et al. [GNKP10] used a *Fresnel-reflection model* to show parts of the culled front faces in order to increase the spatial shape perception: the smaller the angle between a surface normal and the view vector, the higher the transparency. Lawonn et al. [LGP14] additionally emphasized convex and concave regions with an illustrative technique that was inspired by *suggestive contours* (Figure 8a). The method is applicable to arbitrary surfaces and thus suitable for the cardiac anatomy. Van Pelt et al. [VPBB*10] abstracted the surface depiction using a *cel shading* (Figure 8b). Preim et al. [PB13] provided an overview of visualization of vascular structures.

Dynamic Vessels: A depiction of the vessel motion might support the understanding of interdependencies between the pulsatile flow and the dynamic morphology. Furthermore, the increased realism can support patient education and inspire discussions among treating physicians. Lantz et al. [LDE14] performed manual segmentations for each temporal position on additional *balanced steady-state free precession* images using the freely available software *Segment* by Heiberg et al. and Medviso [HSU*10]. They created an initial mesh that was then stretched to match the geometries of every time step. Consequently, the topology was preserved, which also minimized the computational effort in a subsequently performed CFD simulation. Köhler et al. [KPG*15b] used a graph cut-based 4D segmentation (Section 3.3) to obtain meshes of each temporal position, as well as a base mesh representing an upper boundary. Projections from the base mesh onto the time-dependent meshes were then used to obtain a list of displacement vectors for each vertex. This facilitated a constant topology (the base mesh), which allowed a spatio-temporal smoothing of the motion information (the displacement vectors). The dynamic visualization was established using an OpenGL geometry shader. Normal vectors were recalculated in every frame to ensure correct lighting.

4.2. Direct Volume Rendering

A *direct volume rendering* (DVR) can be realized with *raycasting*, which is a common choice nowadays since it is highly parallelizable and thus suitable for GPU computing [KW03]. The TMIP turns out very suitable, since it shows the least noise. Unfortunately, viewing the intravascular flow is limited in standard DVR, since it is not simply possible to make solely the back side of the vessel opaque and the front as well as inner regions transparent. Methods that simulate isosurface visualizations by emphasizing boundaries could use gradients to approximate front face culling. Behrendt et al. [BKP16] proposed a DVR front face culling, where the vessel's back sides are determined during the raycasting.

Instead, a common approach is to employ a *maximum intensity projection* (MIP). This avoids unnecessary algorithm complexity and the specification of a transfer function. Due to the 2D nature of MIP, spatial relations get lost. However, when intravascular flow is shown, the user gets a reasonable impression of the vessel shape (Figure 8c). Venkataraman [Ven10] implemented such an approach as technical demo. A MIP is also suitable for the combination with a geometric mesh, since it can be used as background for the vessel surface rendering (Figure 8d).

5. Qualitative Flow Analysis

Analysis of the vessel shape helps to assess morphology-related pathologies, such as dilations or narrowings. However, the investigation of blood flow characteristics facilitates a deeper understanding of a patient's situation. Segmentations – accurate or approximate – are commonly used to restrict the flow calculation to the inside of the vessel.

Inspired by Post et al. [PVH*03], we explain direct as well as geometry- and feature-based flow visualization techniques in the following. Texture-based are difficult to adapt to time-varying 3D data. Thus, they are rather uncommon in the cardiovascular context and will not be considered.

5.1. Direct Methods

Direct flow visualization techniques are suitable to illustrate basic flow characteristics in a vessel cross-section, whereas 3D and 4D visualizations are rapidly dominated by visual clutter.

5.1.1. Velocity Profile

Blood flow through a cross-section is often color-coded according to the velocities. Rainbow scales are, mostly out of habit, widely used in the medical context, although they might be confusing, obscuring, misleading [BT07] and should be avoided. Yet, they are used as default in most commercial medical image viewers. Other colormaps such as red-blue are often used to depict the flow direction – forward or backward – regarding the centerline tangent or the viewing direction.

Height Fields: The temporal development of the flow profile might be shown in an animation or as a height field (Figure 9a). This allows to draw conclusions on the distribution of high velocities. Height field visualizations were established early on by Paulsen et al. [PH83], who depicted time-varying velocity profiles of canine ascending aortas using data from a hot-film anemometer.

Cross-sectional Patterns: Line or arrow *glyphs* can be helpful to analyze flow patterns in a cross-section (Figure 9b). Laidlaw et al. [LKJ*05] performed a comparison of six different 2D vector field visualizations. Yang et al.

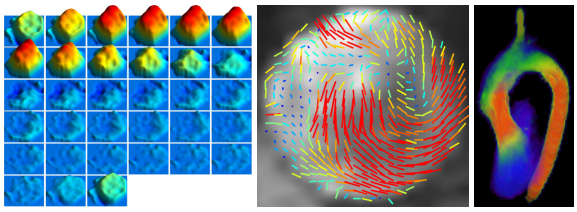

(a) (b) (c)

Figure 9: Direct visualization techniques. (a) The time-dependent flow through a measuring plane is shown as height fields, where height and color represent the velocity. Image based on Heiberg et al. [HSU*10]. (b) Flow pattern in a cross-section depicted via line glyphs. (c) DVR (raycasting) of systolic flow velocities.

[YBKM91] suggested animated arrow maps to depict pulsatile flow.

5.1.2. Direct Volume Rendering of Flow Velocities

A DVR of flow velocities in one time step illustrates the distribution of fast and slow blood (Figure 9c). Masking (Section 3.2) the phase images V is recommended to exclude surrounding noise from the visualization. However, the visualization includes no directional information, a transfer function has to be specified and one has to either find a suitable temporal position to show, such as peak systole, or establish a time-varying DVR.

5.2. Geometry-based Methods

Geometry-based flow visualization techniques depict the course of flow trajectories by means of geometric objects, such as lines or particles. This concept has been widely adopted for the visualization of 4D PC-MRI blood flow.

Buonocore [Buo98] described the visualization of blood flow patterns using *paths* (streamlines, pathlines) and linked abnormal flow patterns to atherosclerosis. Wigström et al. [WEF*99] proposed the simultaneous display of particle traces and morphologic slices to increase the comprehension of intracardiac flow patterns. Calkoen et al. [CRK*14] demonstrated the usefulness of flow visualizations by adjusting the positioning of measuring planes according to qualitatively assessed directions of high velocity flow.

5.2.1. Seeding

A flow trajectory is the solution to an *initial value problem* of an *ordinary differential equation*. Each initial value, which is a 4D *seed point* in the flow field V, will produce one particle path. A *seeding strategy* is a specific scheme to place seed points within the flow domain (here: the vessel). The goal is to minimize visual clutter, while including salient features in the resulting set of trajectories.

Volumetric Seed Point Generation: A *uniform distribution* places *N* 4D seed points at random spatio-temporal positions within the vessel. To ensure that characteristic flow features, such as vortices, are captured, one seed can be placed in *every* voxel in *each* time step, using either the voxel center or another intravoxel random position. A less time- and memory-consuming approach is to guarantee that every voxel is *visited at least once* per temporal position. This can be done by alternating seeding plus integration and then checking which voxels were visited. The density of the resulting line set depends on the dataset's grid resolution. *Entropy-based methods* place seeds in proximity to features, which can be determined by thresholding a corresponding measure such as a vortex criterion.

Planar Seed Point Generation: An *emitter plane*, preferably lying in the vessel's cross-section, facilitates interactive flow exploration. Again, uniform distribution or a specific scheme on the plane can be used. Van Pelt et al. [VPBB*11] proposed a probing tool, which is a truncated cone that fits the vessel at a user-specified location, as trade-off between planar and volumetric seeding.

5.2.2. Trajectory Calculation

The common approach to calculate blood flow trajectories is to use an integration scheme from the *Runge Kutta* family such as the *Dormand-Prince method* (DOPRI5(4)) [DP80]. In combination with hardware-accelerated 3D texture lookups this is suitable for fast GPU computing. If only one temporal position is considered, the integration yields a 3D *streamline*, representing a snapshot of the dynamic flow. Vortex cores of streamlines and pathlines do not necessarily coincide. Thus, only a 4D (3D+time) *pathline* (also: *particle path*) represents true blood flow trajectories in the cardiac cycle. Pathlines can be precalculated in an initialization step, which increases the performance during the visualization (or animation). Another approach is to perform the flow integration in real-time as particle system, where each particle stores a series of recent positions.

5.2.3. Visualization

Geometries: Particles may be visualized as glyphs, such as arrows, spheres, cones [KGP*13] or ellipsoids that are stretched according to the flow velocity [VPBB*11] (Figure 10a). *Pathlets* (also: *trails*) emphasize the development of a trajectory. Temporal information can be mapped to transparency, so that the opacity is decreased for older positions. In this case, *order-independent transparency* (OIT) [YHGT10] is recommended to ensure correct *alpha blending*.

Line Rendering: The pathlines can be shown all at once without employing the temporal information. Techniques such as *illuminated streamlines* (ISL) [ZSH96] and *halos* [IG97, EBRI09] are suitable to enhance the flow visualization. Also, the rendering can be adapted so that the lines always remain orthogonal to the viewer's direction. McLoughlin et al. [MLP*10] provided a corresponding overview. If (semi-)quantitative assessment is the focus, a careful use of line visualization techniques is recommended to avoid distractions (Figure 10b).

Illustrative techniques [EBRI15] might be adapted to the blood flow context, as done by Born et al. [Bor14]. Brambilla et al. provided an overview of illustrative flow visualization techniques [BCP*12].

Line Perception: Forsberg et al. [FCL09] performed a comparison between four 3D integral line renderings: Lines and tubes on monoscopic and stereoscopic monitors. They concluded that the best methods is task-dependent, but lean towards lines on stereoscopic monitors as an overall favorite.

Flow Simplification: Visual clutter is a problem for dense

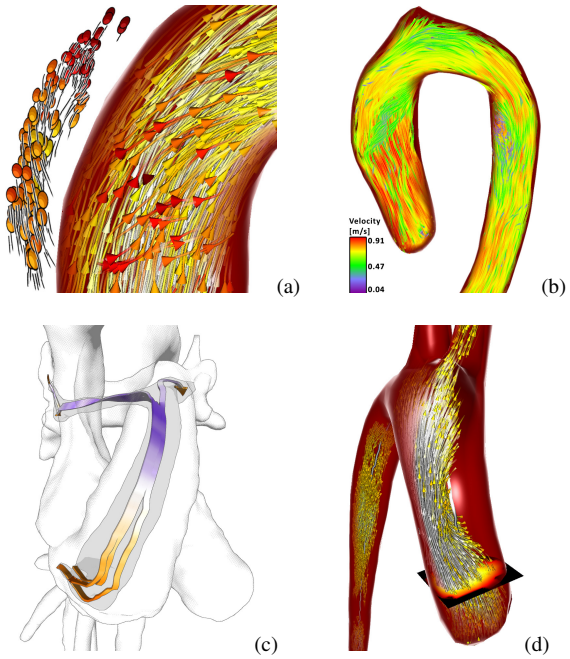

Figure 10: Trajectories are visualized as pathlets (b) with ellipsoids or cones (a) as particle geometries. (c) 3D arrows represent line bundles. (d) Extracted systolic inflow jet.

line sets. Angelelli et al. [AH11] described a vessel straightening to simplify side-by-side visualizations of integral lines of different temporal positions. Van Pelt et al. [VPJtHRV12] performed a hierarchical clustering on the phase image V and generated a representative pathline for each cluster. Born et al. [BMGS13] addressed this problem by creating 3D arrows as representatives of line bundles (Figure 10c). Feedback by two radiologists confirmed the intuitiveness of their method. The neglection of small-scale features was not considered as a disadvantage. The facilitated easier comparison of pre- and postoperative patient data was seen as a clinical benefit.

Flow Animation: A pathlet visualization can also be achieved with precalculated pathlines. Particles (the glyphs) are placed at positions where the current time of the running animation matches the temporal component of the pathline. In addition, only a small time frame around the particle position is shown, i.e., all pathline points with a temporal distance higher than a threshold are hidden. An advantage of precalculated pathlines over on-the-fly-integrated particles is that the exact same paths can be evaluated multiple times. Köhler et al. [KPG*16] proposed *vortex animations with adaptive speed* (VAAS) – a technique that can be described as view-dependent histogram equalization of feature (vortex) visibility in videos by using time lapse and slow motion. Feature visibility is analyzed for each individual video frame by rendering both the vessel mesh and extracted pathlines, which represent the feature of interest, as binary masks, and then forming the ratio of foreground pixels.

5.2.4. Interaction

Manipulation of the current animation time is possible with a slider or simply via pause, stop and play. Line predicates (Section 5.3.1) allow a threshold-based filtering of particular flow properties of interest such as high velocities [BPM*13]. Van Pelt et al. [VPBB*11] proposed a probing tool suitable for a vessel depiction via DVR (Section 4.2). The method facilitates an interactive, qualitative exploration of intravascular flow without a segmentation. Created measuring planes for cross-sectional quantification methods (Section 6.1) are initially placed perpendicularly to the centerline and scaled according to the vessel's cross-section. The user can adjust the position by dragging the plane along the centerline. Vilanova et al. [VPvP*14] provided an overview of further exploration tools for measured and simulated, cerebral and cardiac data.

5.3. Feature-based Methods

Feature extraction is used to simplify visualizations or to investigate specific macroscopic blood flow properties. Therefore, the term *feature* refers to specific flow characteristic, such as high-velocity jets in cardiac vessels. In this section, we put emphasis on salient patterns, since prominent vortical flow behavior is considered as indicator for different cardiovascular pathologies and thus is of great clinical interest.

5.3.1. Line Predicates

Salzbrunn et al. [SGSM08] introduced *line predicates* as Boolean functions that encode if integral lines fulfill certain properties of interest. The filtering criteria are based on line geometries, the underlying flow field V or mesh-related measures such as distances to the vessel wall. A predicate can be applied to whole lines or to the single points of it. In the latter case, lines can be split into fragments. Also, the resulting sets of integral lines from different predicates can be concatenated with common set operations in order to formulate complex queries. Shi et al. [STH*09] described various attributes especially for pathlines. Born et al. [BPM*13] used line predicates to extract different features, such as specific flow paths, jets (Figure 10d) or blood with high *residence times*. Furthermore, they extracted vortices and used predicates to display involved integral lines. Hennemuth et al. [HFS*11] filtered by source and target regions, which yielded a connectivity visualization. Gasteiger et al. [GLvP*12] determined *inflow jets* and *impingement zones* in simulated (CFD) blood flow data of cerebral aneurysms, which shows the high flexibility of line predicates.

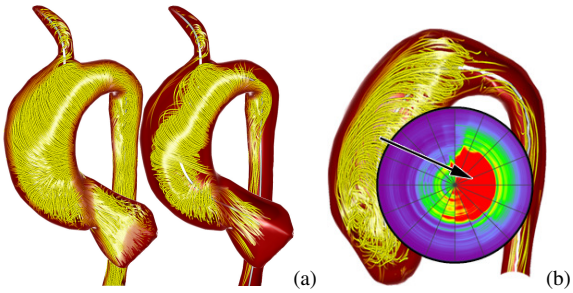

(a) (b)

Figure 11: (a) Pathlines before and after vortex extraction. (b) 2D polar plot as overview of aortic vortex flow.

5.3.2. Vortex Cores

The majority of methods from the flow analysis community is made for 2D or 3D vector fields, and is therefore not directly applicable to 4D PC-MRI data, since flow is inherently time-varying. Evaluating each temporal position independently with a 3D method might introduce errors, since it is not guaranteed that vortices of streamlines and pathlines coincide. Nevertheless, many 3D techniques have been shown to produce reasonable approximations. Stalder et al. [SFH*10] used a combination of the λ_2 *criterion* [JH95] and the *reduced velocity* [SH95] (overview by Jiang et al. [JMT05]) to identify independent points that represent vortex cores mainly in the aorta. Streamlines were seeded in the close surrounding to provide a visual impression of the vortices. Elbaz et al. [ECW*14] employed the λ_2 criterion to extract vortex core rings, which are assumed to be a blood transport mechanism in the left ventricle. However, vortex core extraction is challenging due to noise in the measured data.

5.3.3. Vortex Regions

Clinicians are often more interested in the characteristic of a vortex than topological properties such as core lines [KGP*13]. Consequently, Köhler et al. aimed at extracting visually appealing pathlines with long, continuous, and smooth courses (Figure 11a). They incorporated different local vortex criteria in the line predicates technique and determined the λ_2 criterion as most suitable. Carnecky et al. [CBW*14] further increased noise robustness of the λ_2 calculation by suggesting an orthogonal decomposition of the phase images. The extracted pathlines, which convey vortices, were used to establish a polar plot [KMP*15] as an overview of present vortex flow in the aorta (Figure 11b). The temporal component is mapped to the plot's angle, analogous to a clock, and the course of the centerline is mapped to the radius, starting at the aortic valve location in the center. Meuschke et al. [MLK*16] determined *agglomerative hierarchical clustering* with *average linking* as most suitable to group extracted, vortex representing pathlines.

Left Ventricular Vortex Rings: Elbaz et al. [ELvdG15] pursued an extraction of vortex ring isosurfaces in the left ventricle. They created a scalar field (λ_2 criterion) and computed a reference *shape signature* from a training set using *Euclidean distance shape distributions*. The best fitting isovalue and thus shape of the vortex ring is determined using an iterative search for the best shape distribution match with the reference signature, which is facilitated by a hierarchical clustering.

Vortex Classification: The goal of vortex classification is to find characteristic flow behavior in homogeneous patient collectives. The common approach is to assess vortices manually based on a flow visualization. Hope et al. [HMW*07, HHM*10] counted the total number of vortex occurrences for each dataset and used the following (*mostly binary*) criteria to grade individual vortices:

- The *shape* refers to the elongation of a vortex. If it shows a strong forward movement or *torsion*, it is classified as a *helix*, otherwise as a *vortex*.
- The *size* describes the percentaged extent of vortices in the vessel's cross-section. A *large* (also: *major*) and *small* (also: *minor*) vortex occupies more and less than 50% of the cross-sectional area, respectively.
- The *turning direction* divides the vortex orientation into *left-* and *right-handed*.
- The *temporal occurrence* distinguishes between *systole* and *diastole* – the two phases of the cardiac cycle.
- The *vessel section* describes the spatial occurrence, e.g., the *ascending* or *descending aorta*, the *aortic arch*, the *left* or *right pulmonary artery* or the *pulmonary trunk*.

Boundaries, e.g., between a helical and vortical shape, are not always clear and other criteria, such as the turning direction and size, might be difficult to assess from flow animations or static visualizations. High interobserver variability is the consequence, which makes such manual classification inconvenient for clinical practice [vSCG*15].

5.3.4. Pattern Matching

Heiberg et al. [HEWK03] described *vector pattern matching* (VPM) in order to locate and identify specific 3D flow structures. They analyzed the similarity of normalized flow vectors in a plane to idealized templates via convolution. Each template consists of a pattern, such as right-handedly swirling flow, describing the structure's cross-section and a second perpendicular pattern that is oriented in direction of the structure (Figure 12). The largest eigenvalue of a resulting structure tensor per voxel is used as similarity measure. The computational effort is high, since different rotations of the patterns are used to find the maximum similarity. Furthermore, specification of the templates requires a priori knowledge, e.g., about the forward movement along the vortex core (axial velocity).

Adaptive VPM: Drexl et al. [DKM*13] proposed an adaptive VPM, where candidate voxels are identified using a

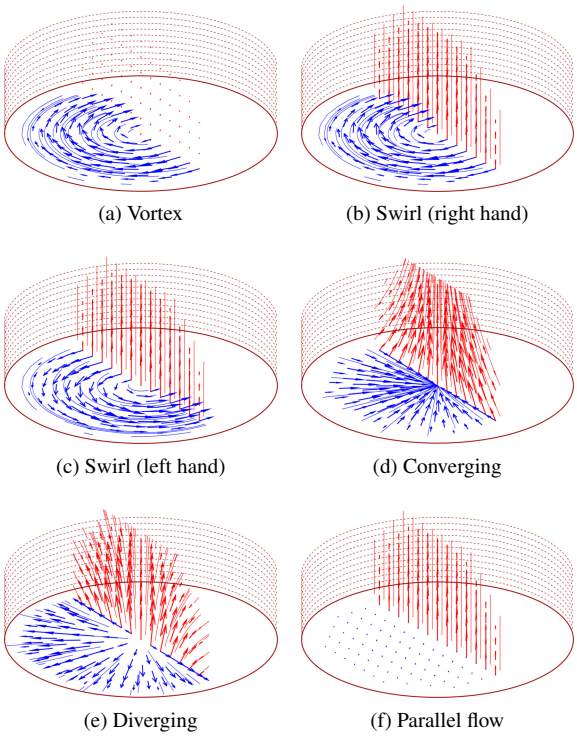

(a) Vortex (b) Swirl (right hand)

(c) Swirl (left hand) (d) Converging

(e) Diverging (f) Parallel flow

Figure 12: Six idealized templates used for vector pattern matching. The **blue pattern** lies in the cross-section, whereas the **red pattern** shows a cut view along the **vessel** (adumbrated as **surrounding circle**). Images based on Heiberg et al. [HEWK03].

threshold on the vorticity magnitude $||\vec{\omega}||$. The vortex core orientation is then estimated with the vorticity vector $\vec{\omega}$, and templates are rotated accordingly. Adaptive VPM is 50% faster than VPM, shows increased robustness, and has a simplified template specification, since it needs only one template for the detection.

Pattern Parametrization: Van Pelt et al. [VPFCV14] proposed a VPM-based blood flow characterization. They defined a single parameter $\in [0,1]$ that is sufficient to describe patterns in the plane and thus characterize helical and vortical flow behavior.

6. Quantitative Flow Analysis

Quantitative measures are essential to assess the severity of pathologies or to support treatment decisions. For example, the *stroke volume* helps to assess the heart's pumping capacity. Pathologically low values might indicate heart failure. Stenotic vessels typically show a *pressure drop*, i.e., there is a high and low pressure before and after the narrowed region, respectively. The re-evaluation of *pressure gradients*, e.g., after a balloon dilatation (widening of the vessel), may improve the judgment of a patient's post-treatment situation. Moreover, quantitative measures facilitate the establishment of comprehensive visualizations of a patient's situation. Hope et al. [HSD13] provide an overview of such measures with emphasis on the clinical importance, whereas we focus on technical aspects in this section.

6.1. Cross-sectional Methods

Measuring planes that are modeled as discrete grids, are the basis for many quantifications. An accurate determination of the lumen pixels – the pixels inside the vessel – is required (Section 3.4). A plane can be aligned orthogonally to the vessel using time-averaged flow vectors, analysis of local structure tensors [VPBB*10] as estimation of the vessel course or, if available, the centerline direction.

Measuring Plane Placement: Measuring planes can be evaluated at arbitrary positions, which might impede result comparison between different datasets. Therefore, Schulz-Menger et al. [SMBB*13] proposed a standardization of the postprocessing and data evaluation. Among others, they suggested ten measuring plane locations in the aorta based on anatomical landmarks.

6.1.1. Flow Rate

The *time-dependent flow rate* $fr(t)$ [ml/s] describes the orthogonally passing blood flow through a plane P with the normal vector $\vec{n} \in \mathbb{R}^3$, scale $\vec{s} = (s_x, s_y)$ [mm] per cell and grid size $\vec{g} = (g_x, g_y)$:

$$fr(t) = s_x \cdot s_y \cdot \vec{n} \cdot \sum_{x=0}^{g_x\text{-}1} \sum_{y=0}^{g_y\text{-}1} S(P(x,y),t) \cdot \mathrm{V}(P(x,y),t) \quad (5)$$

$$\text{with} \quad S(P(x,y),t) = \begin{cases} 1, & P(x,y),t \text{ inside vessel} \\ 0, & \text{else} \end{cases}$$

$P(x,y) = \vec{p}$ is a position on the plane transformed to 3D world coordinates. $\mathrm{V}(P(x,y),t)$ [m/s] yields velocity vectors $\vec{v}$ from the phase image V. If calculated for each temporal position, $fr(t)$ is periodic, since it represents one full heartbeat (Figure 13a).

Flow Volumes: The *forward flow volume* (FFV) [ml] and *backward flow volume* (BFV) [ml] is the area of the $fr(t)$ curve above and below 0, respectively, scaled with 10^{-3} to obtain [ml]. The *net flow volume* (NFV) [ml] is FFV−BFV or simply the integral of $fr(t)$. Thus, the NFV can be positive or negative, depending on whether forward or backward flow is predominant [KFU*87, BB94]. The *stroke volume* (SV) [ml] describes the pumped blood per heartbeat and thus helps to assess the cardiac function. It is a special case of the NFV, where the measuring plane is located directly above the aortic or pulmonary valve. The *percentaged back flow volume* (PBFV) [%] is the ratio BFV/(FFV + BFV). The *regurgitation fraction* (RF) [%] is the PBFV measured

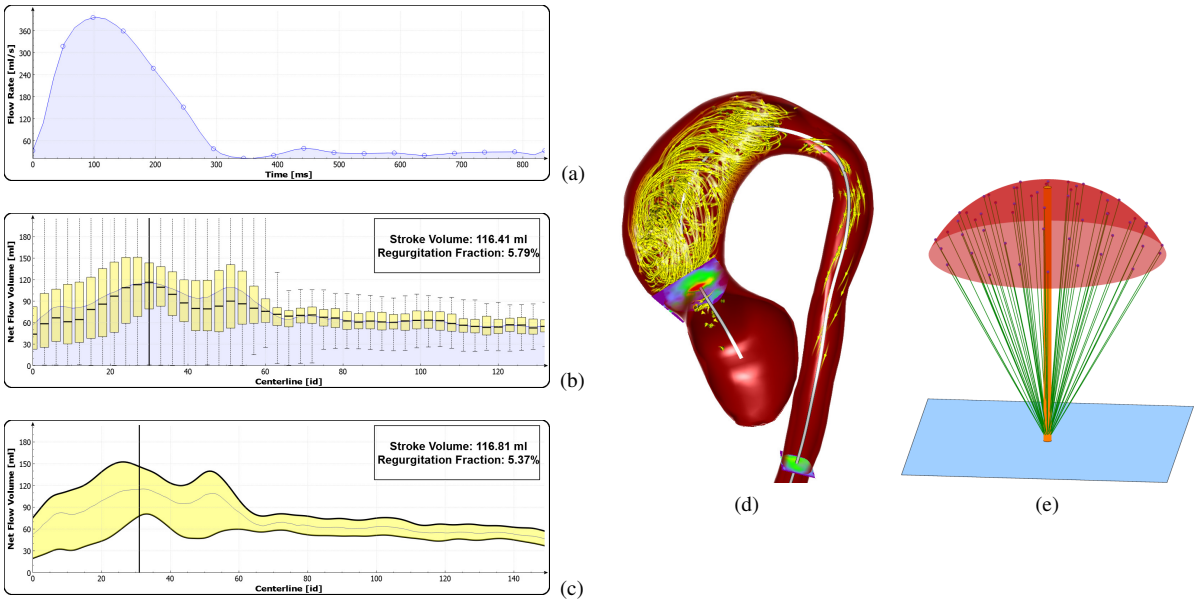

Figure 13: (a) Flow rate curve $fr(t)$ from a measuring plane in the ascending aorta of a healthy volunteer. (b–e) Robust net flow volume (NFV) determination along the vessel. Equidistant planes on the vessel's centerline between two given locations (planes in (d)) are analyzed. For each centerline position: Different **plane** (**blue**) **angulations** (**green**) (e) are evaluated, the resulting NFVs distribution are shown as box plots (b). The x-axis of the plot starts at the approximate aortic valve location and then follows the vessel course. (c) Adapted visualization where only the interquartile ranges (middle 50% of the values) are shown. Due to the patient's heavy systolic vortex flow (d), the NFV quantification is uncertain in the ascending aorta.

directly above the aortic or pulmonary valve and thus describes the percentage of blood flowing back when the corresponding valve should be closed. RFs below 5% can also occur in healthy persons and are considered as physiological [WKS*09].

Inaccuracies: Hoogeveen et al. [HBV99] pointed out the susceptibility of the flow rate calculation to different imaging artifacts. They suggested a model-based approach that is applicable to small, straight, and cylindrical arteries with a parabolic velocity profile. Therefore, this is not suitable for the cardiac context. Köhler et al. [KPG*15c] determined vortex flow as a main cause for quantification uncertainties. They suggested a systematic evaluation of measuring planes with slightly different angulations, which yields a distribution of NFVs. A box plot-based graph illustrates the result variations (Figures 13b–13e).

6.1.2. Pulse Wave Velocity

The *pulse wave velocity* PWV [m/s] [BH22, McD68] is an indicator for arterial stiffness, since it is lower and higher in elastic and stiff vessels, respectively. Stiffness increases with age as well as various physiological, genetic, and cardiovascular risk factors [HSD13]. We follow Wentland et al. [WGW14] and Dyverfeldt et al. [DEL14] who both provided overviews of MRI-based PWV measurements, which were first discussed by Mohiaddin et al. [ML89]. Markl et al. [MWB*10] focused directly on 4D PC-MRI in their overview. Originally, PWV is computed using the *Moens-Korteweg* equation:

$$\mathrm{PWV} = \sqrt{\frac{E \cdot h}{2 \cdot r \cdot \rho}}\,, \tag{6}$$

where E [kg/(m·s^2)] is the vessel's *elastic* (also: *Young's*) *modulus*, h [m] is the wall *thickness*, r [m] is the vessel *radius* and ρ [kg/m^3] is the blood *density*.

PWV for MRI: The MRI-based calculation directly relates to the development of the flow curve (also: *wave* due to its typical appearance) along the vessel's course:

$$\mathrm{PWV} = \frac{\Delta d}{\Delta t}\,, \tag{7}$$

Δd [m] describes the intravascular distance (length of the centerline) between two measuring planes (Figure 14a) and Δt [s] is the temporal offset of the flow rate $fr(t)$ curves (Figure 14b). The offset between two waves can be obtained using specific landmarks (Figure 14c) or by comparing whole curves:

- *Time-to-peak* (TTP) uses the curves' global peak as landmark. This is prone to errors, since the actual peak can easily be missed due to the limited temporal data resolution.

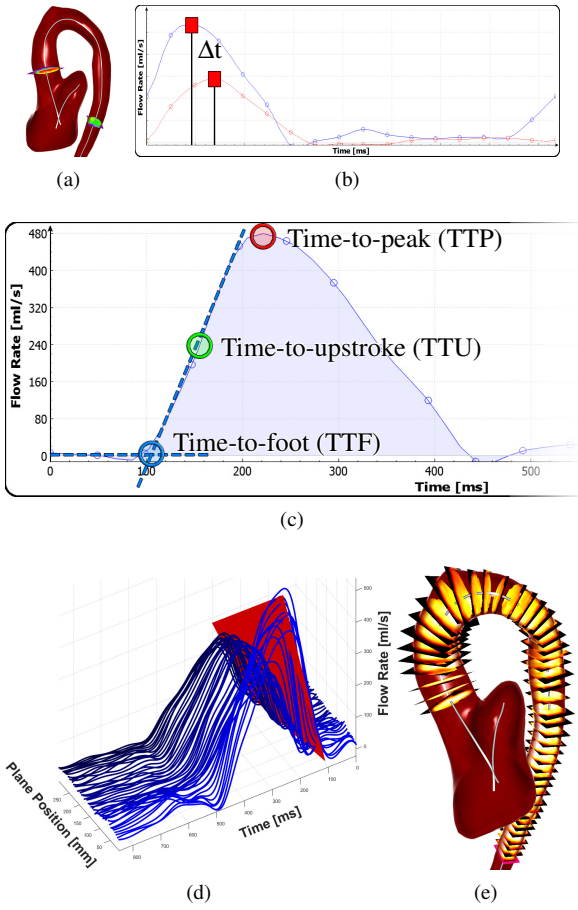

(a) (b) (c) (d) (e)

Figure 14: (a–b) Temporal offset of the flow curve between measuring planes in the ascending and descending aorta. (c) Depiction of **time-to-foot** (TTF, **blue**), **time-to-upstroke** (TTU, **green**) and **time-to-peak** (TTP, **red**). Images based on Wentland et al. [WGW14]. (d) **Regression plane** (**red**) fitted to the upstrokes of multiple flow curves along the aorta (e). Image based on Spottiswoode et al. [SSG*13].

- *Time-to-foot* (TTF) (also: *zero crossing*) [MR93, BBSS00, YPW*06] fits a regression line to the upstroke of the waveform and then determines its intersection with either the baseline ($fr(t) = 0$) or another regression line prior to the upstroke. Often, only data points between 20% and 80% of the maximum value are considered [WGW14]. A variation of TTF is to use the time on the fitted line where the velocity corresponds to, e.g., 20% or 50% of the peak velocity (*threshold method* (TH)).
- *Time-to-upstroke* (TTU) (also: *derivative method*) uses the time of the wave's first derivative peak value as landmark [ABT*95].
- *Sigmoid fitting* approximates a sigmoid function describing the wave's upstroke [DRL*11]. The temporal distance between the sigmoid functions is determined by comparing the positions with the highest curvature.
- *Cross-correlation* (XCorr or just XC) [FFJH*08] performs incremental temporal shifts of one waveform and uses the temporal offset as result where two curves' correlation was highest.
- The *Fourier analysis* (FA) *method* is used to determine two waves' phase shift by fitting a line to low frequency components of the Fourier transformed waves [LHKS88]. The temporal distance is derived from the slope of this regression line.
- The *center of mass* (COM) [DEL14] is calculated as weighted average of points on the curve that are located between 20% of the peak flow rate on the upslope and 20% of the peak flow rate on the downslope of the wave.

Performance: Methods that operate on the upslope (TTP, TTF, TH, TTU, sigmoid fitting) tend to produce lower values than methods that incorporate global wave information (XCorr, FA, COM). Thus, Dyverfeldt et al. [DEL14] suggested a careful interpretation of PWV values depending on the employed technique. Comparing TH, TTF and TTU Mirzaee et al. [MDHH13] determined TH as most robust. Wentland et al. [WWF*13] reported similarly reliable results of TTU, TTF and XCorr compared to TTP as well as a good agreement of PWV obtained with 2D and 4D PC-MRI.

Robustness: Often, the PWV is obtained using more than two planes. In this case, Δd and Δt are calculated between each plane sample and the first plane. The inverse slope of a fitted regression line yields the PWV. Drexl et al. [DKM*13] described a PWV calculation, where the user simply defines a start and end position on the centerline and equidistant planes are generated (Figure 14e) and evaluated automatically. Spottiswoode et al. [SSG*13] and Magrath et al. [MMS*14] achieved increased robustness by fitting second order polynomial planes to a series of flow curves' upstrokes (Figure 14d).

Drawbacks: A general problem of the PWV quantification is its strong dependency on typically shaped, noise-free flow rate curves (Figure 13a). Noise or an ambiguous peak value can lead to implausible results. Especially pathologic cases with vortex flow are likely to produce aberrant flow rate curves depending on the respective measuring plane configurations [KPG*15c]. Dyverfeldt et al. [DEL14] restrict the PWV quantification to the descending aorta, since the flow rate calculation is more reliable there.

6.1.3. Flow Displacement

The normally parabolic velocity profile can be disrupted by vortex flow patterns or disturbed valve opening characteristics. To quantify *eccentric flow jets*, Sigovan et al. [SDW*15] defined *flow displacement* $\in [0, 1]$ in a cross-section as distance between the center position and the "center of velocities", which is the velocity-weighted average of all positions in the plane, normalized with the vessel diameter (Figure

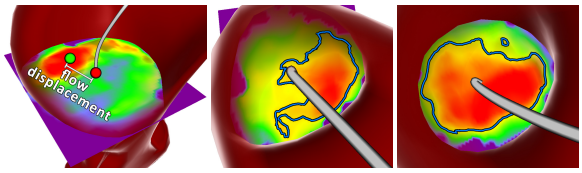

(a) (b) (c)

Figure 15: (a) Flow displacement in a cross-section as difference between the **center position** (**red**) to the **"center of velocities"** (**green**). (b–c) More (b) and less compressed (c) distribution of **high systolic flow velocities** (framed in **blue**).

15a). Kari et al. [KKB*15] defined the *flow compression index* $\in [0,1]$ as fraction of the area of mid-systolic high velocity flow and the total area of the aorta's cross-section.

6.2. Surface-based Methods

Surface-based measures describe fluid-vessel wall-interactions and the resulting effects on the vascular wall. Research on this mutual influence can increase the understanding of the initiation and progression of related vascular diseases. Corresponding calculations typically depend on an accurate vessel segmentation and geometry.

6.2.1. Wall Shear Stress

Wall shear stress (WSS) [Pa] represents the force tangential to the inner layer of the vessel wall caused by nearby, complex blood flow. A WSS vector $\vec{\tau}_{WSS}$ describes the corresponding direction of the shear force (*shear stress*). Recent research suggests that exposure to increased shear forces over a long period of time promotes pathologic vessel dilations [BSK*14] (Figure 16c).

WSS is a *time-resolved* measure, calculated as the product of the *shear rate* $\dot{\gamma}$ [1/s] and the *dynamic viscosity* μ [Pa·s]. The latter describes the blood's resistance to gradual deformation by shear stress and is often chosen as $10^{-3} \cdot 3.5$ [PS05] or $10^{-3} \cdot 3.2$ Pa·s [WSN10] for large arteries. However, $\dot{\gamma}$ has to be derived from the measured flow. In some applications, WSS is *time-averaged*, calculated at only one specific temporal position such as peak systole or the *maximum* WSS during the cardiac cycle is projected.

Papaioannou et al. [PS05] provided an overview of basic principles of and methods for vascular WSS. While WSS can be obtained from CFD blood flow simulations (Section 7) with a very fine grid in near-wall vessel regions, it is more challenging to reliably compute it based on measured flow data. We follow Potters et al. [PMVN14] who specifically described different MRI-based calculations. In addition to reliable flow measurements, especially in proximity to the wall, all WSS methods require an accurate segmentation of the vessel lumen or, more precisely, the vessel wall.

WSS Approximation on a Boundary Curve: If a single slice is evaluated, the resulting WSS corresponds to the cross-section's boundary curve, which equals a ring on the vessel surface. Simple approximations determine a mean WSS value WSS_{avg} for the whole curve using the *Poiseuille* formula [MAI99]:

$$WSS_{avg} = \mu \cdot \dot{\gamma} = \mu \cdot \frac{4 \cdot Q}{\pi \cdot r^3} \tag{8}$$

or similar velocity-based formulae such as:

$$WSS_{avg} = \mu \cdot \frac{4 \cdot ||\vec{v}||_{avg}}{r} \quad \text{or} \tag{9}$$

$$WSS_{avg} = \mu \cdot ||\vec{v}||_{max} \cdot \sqrt{\frac{2 \cdot \pi \cdot ||\vec{v}||_{max}}{Q}} \quad , \tag{10}$$

where Q [m^3/s] is the mean *volumetric flow rate*, r [m] is the radius and $||\vec{v}||_{avg}$ [m/s] and $||\vec{v}||_{max}$ [m/s] is the average and maximum velocity, respectively. Such methods assume that the flow is steady and laminar and the vessel is straight, cylindrical and inelastic [PS05], which is especially problematic for pathologic cases.

More sophisticated approaches incorporate the actual measured flow profiles in the WSS calculation. Oshinski et al. [OKML95] plotted sampled velocities in the plane against the distance of the corresponding pixels to the vessel wall. The slope of a linear regression line yields the required shear rate $\dot{\gamma}$. The use of a parabolic instead of linear function for the fitting might increase the accuracy [MFU*99].

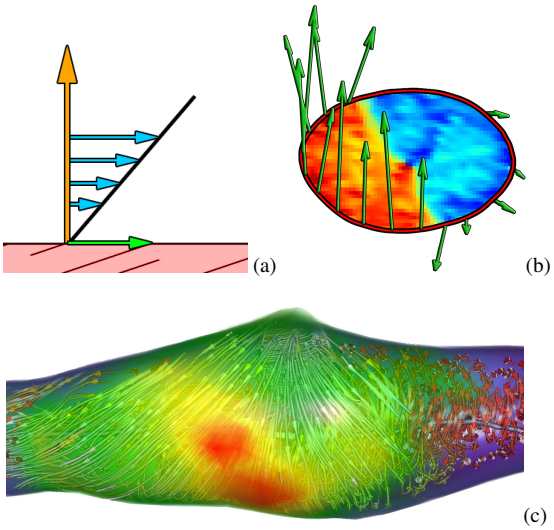

(a) (b) (c)

Figure 16: (a) **Velocity vectors** (**blue**) that are sampled along the **normal vector** (**orange**) are used to obtain the **wall shear stress vector** (**green**) on the **vessel surface** (**red**). (b) $\vec{\tau}_{WSS}$ on the **vessel contour** (**red**) on a measuring plane. (c) Flow impinges on the vessel wall and causes increased WSS.

Oyre et al. [ORK*98a, OPR*98, ORK*98b] derived the WSS from a 3D paraboloid fitted to large parts of the velocity profile. They excluded pixels close to the wall and in the center. Cheng et al. [CPT02] employed analytical velocity derivatives along the inward pointing normal, which are facilitated by local velocity profile approximations via *Lagrangian base functions*.

WSS Vectors $\vec{\tau}_{WSS}$ on a Boundary Curve: Newer WSS methods incorporate the additional information provided by 4D PC-MRI data (Figure 16b). Köhler et al. [KMR*01] and Papathanasopoulou et al. [PZK*03] fitted a fifth order polynomial to the whole 3D velocity profile of subsequent slices in a bifurcation phantom in order to derive $\vec{\tau}_{WSS}$. Stalder et al. [SRF*08] manually defined measuring planes inside the aorta and performed cross-section segmentations. $\vec{\tau}_{WSS}$ were derived from B-Splines that were fitted to the velocity values on the segmentation boundary, which represents the vessel wall. Sotelo et al. [SUV*15] proposed a method based on finite elements where $\vec{\tau}_{WSS}$ were obtained from a global least-squares stress-projection. Their technique is suitable for arbitrary plane sections of the thoracic aorta.

WSS Vectors $\vec{\tau}_{WSS}$ on the Whole Surface: Bieging et al. [BFW*11] introduced a method to obtain $\vec{\tau}_{WSS}$ on each position of a 3D vessel geometry. Consequently, a segmentation of the whole dynamic vessel instead of just a cross-section is required. 3D approximations from a TMIP or similar are often used for convenience (Section 3.2). Potters et al. [PVOVN12, PMVN14] used the term *vectorial* or *volumetric* WSS, which is defined as:

$$\mathrm{WSS} = ||\vec{\tau}_{WSS}|| \qquad \text{with} \tag{11}$$

$$\vec{\tau}_{WSS} = \mu \cdot \dot{\gamma} = \mu \cdot \frac{\partial \vec{v}_{||}}{\partial \vec{n}} \,, \tag{12}$$

where $\vec{n}$ is the normal vector of the corresponding surface mesh position and $\vec{\tau}_{WSS}$ represents the *shear stress* [Pa]. Velocity vectors $\mathrm{V}(\vec{p}_t) = \vec{v}$ are obtained along the inward pointing normal $-\vec{n}$ with the number of samples as well as the maximum distance from the surface point as parameters [PvOM*15]. An orthonormal basis $\{\vec{n}, \vec{n}_x, \vec{n}_y\}$ is used to obtain vectors $\vec{v}_{||}$ that are parallel to the surface's tangential plane:

$$\vec{v}_{||} = \vec{v} - (\vec{v} \cdot \vec{n}) \cdot \vec{n} \tag{13}$$

The first derivatives of the $\vec{v}_{||}$ samples are calculated analytically and evaluated at the vessel wall [VOPG*13] (Figure 16a). One-dimensional, interpolating, cubic B-splines with natural boundary conditions can be fitted to the x and y component of $\vec{v}_{||}$ for this purpose.

6.3. Grid-based Methods

Grid-based techniques operate directly on the acquired image data or solve *differential equations* in *finite elements*.

6.3.1. Pressure Gradients

In case of narrowed (*stenotic*) vessels or valves, blood has to pass a smaller cross-sectional area or valve orifice. Increased flow velocities and intravascular pressure are the consequence. Thus, the blood's *relative pressure* p [mmHg] is an important factor to grade the degree of stenosis (Figure 17).

Bernoulli: The *simplified Bernoulli equation* allows to estimate *pressure gradients* Δp based on the maximum velocity $||\vec{v}||_{\max}$ [HBTA78]:

$$\Delta p = 4 \cdot ||\vec{v}||^2_{\max} \tag{14}$$

Due to the quadrature this is highly sensitive to measurement errors. Oshinski et al. [OPM*96] discussed further drawbacks such as not considering the vessel shape.

Navier Stokes / Poisson: For blood, which is a viscous, incompressible, laminar, Newtonian fluid, Δp can be derived using the *pressure Poisson equation* (PPE, Equation 15), which is based on the *Navier-Stokes equation* [YKW*96,

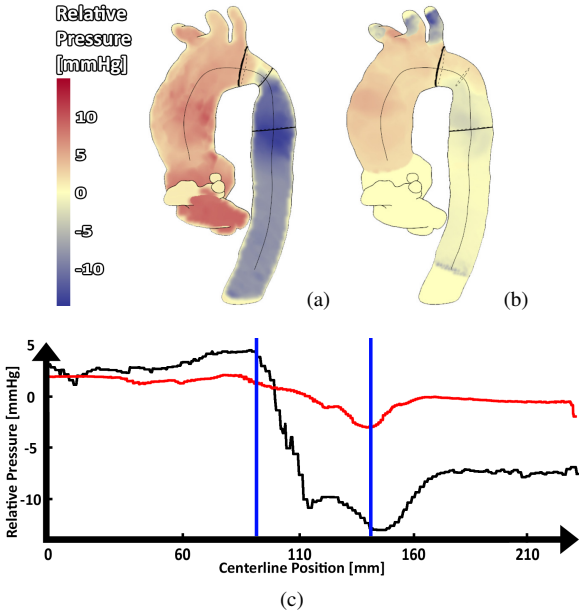

Figure 17: Relative pressure in a patient with aortic coarctation (pathological narrowing of the aortic arch). Pressure drop derived from 4D PC-MRI data (a) and simulated patient situation after treatment (b). (c) Pressure along the centerline. The **black** and **red curve** show (a) and (b), respectively. The **blue enclosure** is the aortic arch region, marked with **black cross-sections** in (a) and (b). Images provided by M. Neugebauer. Image data are courtesy of Prof. Dr. Titus Kühne, German Heart Center. The pressure visualization technique was established by Schumann et al. [SH15].

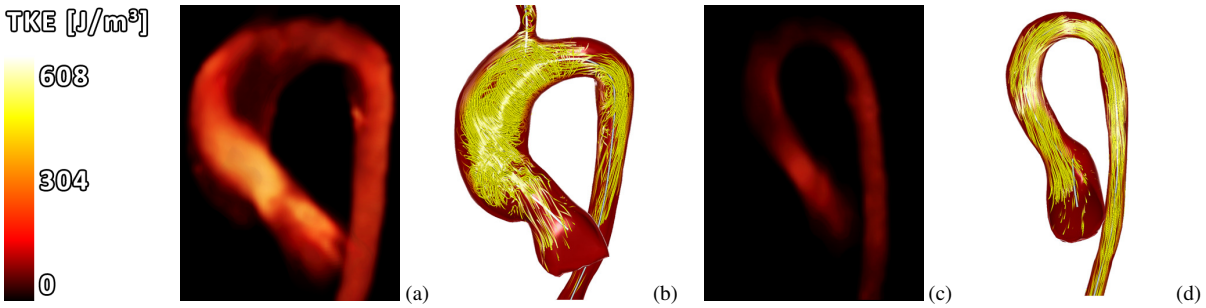

Figure 18: TKE in a patient with heavy systolic vortex flow in the ascending aorta (a–b) and in a healthy volunteer (c–d).

EWB*01]:

$$-\Delta p = \nabla \cdot \left(\rho \cdot \frac{\partial \vec{v}}{\partial t} + \rho \cdot (\vec{v} \cdot \nabla) \cdot \vec{v} - \mu \cdot \nabla^2 \vec{v} \right) \qquad (15)$$

The divergence-free condition must be met due to the fluid incompressibility, where $\nabla \cdot \vec{v} = 0$. $\rho = 1060$ [kg/m^3] is the fluid *density* [BFL*11], $\mu = 10^{-3} \cdot 3.2$ or $10^{-3} \cdot 3.5$ [Pa·s] is the *dynamic viscosity*, $\vec{v}$ [m/s] are velocity vectors from the flow field V and t [s] is the time. Gravitational forces can be neglected due to the horizontal patient positioning in the scanner.

Tyszka et al. [TLAS00] described an iterative PPE solver that has been shown to produce a good agreement with expected values in phantoms and with values of healthy volunteers from the literature [BFL*11]. Ebbers and Farnebäck [EF09] proposed a *multi-grid finite-difference scheme* to solve the PPE directly in the segmented vessel. Meier et al. [MHF*10, MHD*13] exploited properties of hexahedral voxel grid elements to simplify the incorporation of these boundary conditions and being able to use efficient conjugate solvers due to a symmetric system matrix. Itu et al. [ISG*12] solved a 1D Navier-Stokes equation numerically with patient-specific boundary conditions to obtain the pressure distribution along the vessel's centerline. Mihalef et al. [MRG*14] described a method that uses enhanced geometric models, which provide better accuracy than voxel masks of the vessel. Physiologically meaningful boundary conditions are established via tagging of inlets and outlets. Lamata et al. [LKN*14] described a separate evaluation of the transient $\rho \cdot \frac{\partial \vec{v}}{\partial t}$, convective $\rho \cdot (\vec{v} \cdot \nabla) \cdot \vec{v}$ and viscous component $-\mu \cdot \nabla^2 \vec{v}$ (Equation 15), which is based on the finite-element method by Krittian et al. [KLM*12]. They identified transient effects, which originate from the acceleration of the blood, as main cause for relative pressure in the aorta. Donati et al. [DNSL14] paid special attention to the viscous component. They automatically fit a tubular mesh in near-wall regions, where the signal-to-noise ratios are lowest, and reconstruct the vector field there. This improves the computation of the required second order derivatives. In other work, Donati et al. [DFS*15] derived pressure differences using the *work-energy equation* for Newtonian fluids.

6.3.2. Turbulent Kinetic Energy

Parts of the blood's kinetic energy is irreversibly converted into heat due to viscous friction. An elevated level of lost energy increases the heart's workload and might enhance the risk of ventricular hypertrophy (enlargement). Thus, quantification of the energy loss might be a marker for disease severity [ATY08, BvOB*14].

Turbulent Flow: Flow turbulences are irregularities and velocity fluctuations of the blood flow. After turbulences were studied in the aorta with a hot-film anemometer [NS72, SS76], they were considered as potential cause for such energy loss [Cla76]. Dyverfeldt et al. [DSKE06] described *intravoxel velocity standard deviations*. They are the basis for *turbulent kinetic energy* (TKE) [J/m^3], which is a direction-independent measure of turbulence intensities [DKS*08] (Figure 18). It was exploited that turbulent flow attenuates the signal in the 4D flow measurements. A *Reynolds decomposition* of the velocity field V, which is given by the phase images $V_{\{x,y,z\}}$, yields a separation into a mean $\overline{V}$ and fluctuating velocity field V', so that $V = \overline{V} + V'$. Assuming a Gaussian distribution, the kinetic energy of the velocity fluctuations (the TKE) corresponds to:

$$\mathrm{TKE} = \frac{\rho}{2} \cdot \left(\sigma_x^2 + \sigma_y^2 + \sigma_z^2 \right), \qquad (16)$$

where $\sigma^2_{\{x,y,z\}}$ [m^2/s^2] is the variance of velocities in $V_{\{x,y,z\}}$ and ρ [kg/m^3] is the fluid *density* [BKM*13]. Binter et al. [BGHK15] showed that TKE calculation has a relatively low sensitivity to the spatial data resolution.

Carlsson et al. [CHTA12] quantified kinetic energy (KE) [mJ/ml] in the left and right ventricle in a similar way:

$$\mathrm{KE} = \frac{||\vec{v}||^2}{2} \cdot m \qquad (17)$$

The *mass* m of blood in the voxel is calculated as volume of the voxel multiplied with the blood density ρ, which was set to 1.05 [g/ml].

6.3.3. Vortex Strength

The *vorticity* $\vec{\omega}$ (also: *curl*) of a vector field $\nabla \times \mathrm{V}$ describes local spinning vectors:

$$\vec{\omega} = \nabla \times \mathrm{V} = \begin{pmatrix} \frac{\partial w}{\partial y} - \frac{\partial v}{\partial z} \\ \frac{\partial u}{\partial z} - \frac{\partial w}{\partial x} \\ \frac{\partial v}{\partial x} - \frac{\partial u}{\partial y} \end{pmatrix}, \tag{18}$$

where $\vec{v} = (u, v, w)^{\mathrm{T}}$ are velocity vectors. The *vorticity magnitude* $||\vec{\omega}||$ [1/s] is a measure for rotational strength. Wong et al. [WKW*09] visualized slices through the heart chambers using streamline plots colored by the flow velocities, and vector as well as contour maps depicting the vorticity magnitudes. They analyzed the mean vorticity and/or vorticity for each temporal position and depicted the results in a histogram. In addition, they defined a circulation measure as line integral of the tangential velocity along a circuit enclosing a point of interest [WTK*10]. Hess et al. [HBG*13] described *circulation* as fraction of the integral of vorticity magnitudes in an intra-aortic cross-section and the corresponding cross-sectional area. Bächler et al. [BPS*13] plotted maximum absolute vorticity magnitudes over time for measuring planes inside a vessel.

Von Spiczak et al. [vSCG*15] presented 2D and 3D metrics to quantify vortex flow in the thoracic aorta. Six standardized ROIs throughout the aorta were analyzed for minimum, maximum and average vorticity magnitudes (Figure 19). An adapted predictor-corrector method [BS94] in combination with the λ_2 vortex criterion was used to extract vortex core lines. The cores were evaluated regarding their strength and elongation over time. Additionally, surrounding vorticity magnitudes were radially sampled for each core line position using eight lines perpendicular to the core. The sampling stops when $||\vec{\omega}||$ falls below a given threshold.

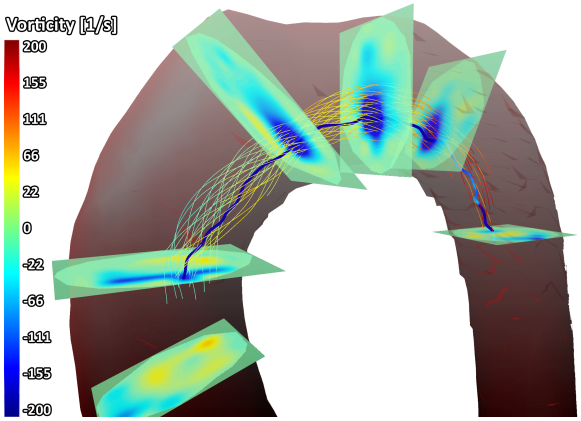

Figure 19: Vorticity analysis at six standardized planes inside the thoracic aorta of a healthy volunteer [vSCG*15]. Image provided by J. von Spiczak.

They defined a vortex' *radial expansion* as the circle's area with a radius equal to the average length of the eight lines.

Helicity: Lorenz et al. [LBB*14] calculated averaged *helicity density* H_d and *relative helicity* H_r for equidistant measuring planes inside the aorta as:

$$H_d = \vec{\omega} \cdot \vec{v} \qquad \text{and} \qquad H_r = \frac{H_d}{||\vec{\omega}|| \cdot ||\vec{v}||} \tag{19}$$

Morbiducci et al. [MPR*09] proposed a *helical flow index* as the average of *local normalized helicity* along pathlines. This is equal to H_r from Equation 19. Averaging the values of all pathlines yields a global assessment of present helicity in the dataset.

6.3.4. Lagrangian Coherent Structures

Lagrangian coherent structures (LCS) facilitate the creation of surfaces, e.g., at vortex boundaries, that divide flow into regions with different characteristics. Based on this, Töger et al. [TKC*12] established a volume quantification of vortex rings (Section 5.3), which are assumed to be a blood transport mechanism in the left ventricle.

FTLE: LCS are based on *finite-time Lyapunov exponents* (FTLE), which describe the rate of separation of nearby particles when integrated for a certain time frame Δt. A *flow map*, usually with a higher resolution than the acquired image data, contains the end positions of particles that started at the spatio-temporal positions $\vec{p}_t$ and were integrated for Δt. The FTLE is defined as:

$$\mathrm{FTLE}(\vec{p}_t) = \frac{1}{\Delta t} \cdot \log\left(\lambda(\vec{p}_t)\right) \tag{20}$$
$$\text{with} \quad \lambda(\vec{p}_t) = \sqrt{\lambda_{\max}\left[J(\vec{p}_t)^{\mathrm{T}} \cdot J(\vec{p}_t)\right]}$$

J is the Jacobian matrix and $\lambda_{\max}$ the maximum eigenvalue.

Krishnan et al. [KGG*12] directly employed the FTLE as a stop criterion for particle path calculations (Section 5.2). If the FTLE is determined close to the vessel boundaries, some of the nearby particles will be seeded inside and some will be placed outside the vessel. Thus, some particles follow the intravascular flow and some will experience a "random" movement due to low velocities and/or arbitrary directions outside

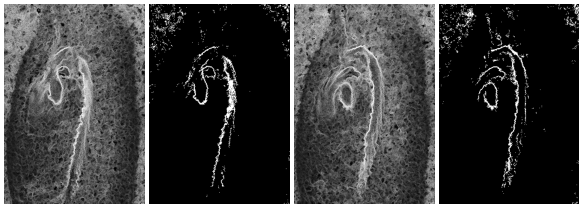

(a) (b) (c) (d)

Figure 20: The application of a threshold (b,d) on FTLE images (a,c) provides an estimation of the vessel boundaries.

the vessel. The resulting high separation allows to estimate the vessel boundaries via thresholding (Figure 20). Unfortunately, the boundary FTLE values depend on the flow velocities and thus may vary for different vessels.

6.3.5. Connectivity

The *connectivity* is calculated as the number of pathlines that pass two specific ROIs [HFS*11]. Problems may arise if the integral lines represent wrong paths due to noise, offset errors or partial volume effects. There is a strong similarity to *diffusion tensor imaging* and the related *fiber tracking*, where probabilistic approaches are employed to calculate paths in uncertain crossings of two or more fiber bundles.

Uncertainty: The connectivity is also used to establish an uncertainty quantification of the integration. Friman et al. [FHH*10] introduced a probabilistic approach that employs a sequential *Monte Carlo* sampling. Schwenke et al. [SHFF11] incorporated an estimated uncertainty tensor into a *fast marching* method and calculate blood flow trajectories as minimal paths.

7. Blood Flow Simulations

Besides MRI-based measurements, flow data can be obtained using *computational fluid dynamics* (CFD). Numerical flow simulations require the specification of various boundary conditions, which is often based on assumptions. For example, it is assumed that flow at the vessel wall is at 0 m/s. In addition, information about the inflow and outflow velocity profile are necessary. Among others, CFD simulations are useful to predict the potential outcome of a treatment like valve replacement or stenting [NGG*15].

Data Assimilation: While 4D PC-MRI data suffer from a limited spatio-temporal resolution, noise and different image artifacts, it is not clear to what extent CFD data truly represent a patient's situation, since the simulations rely on various model assumptions. However, *data assimilation* allows to link the methods and taking advantages of both. A combined approach can be seen as patient-specific simulation, where the measured data are employed as input, or as 4D PC-MRI data with enforced model assumptions, such as zero divergence.

Lantz et al. [LGK12] increased the accuracy of the required CFD boundary conditions. WSS was decomposed into pulsating and fluctuating parts to increase the understanding of WSS on the aortic wall. Renner [Ren11] quantified subject-specific wall shear stress, which refers to corresponding aortic geometries extracted from MRI data. De Hoon et al. [dHvPJV14] presented a fluid simulation where MRI and CFD are coupled in order to exploit the benefits of both methods and improve the visual analysis of hemodynamics.

Verification: Petersson et al. [PDE12] have shown that WSS peak locations obtained from simulated CFD and measured 4D PC-MRI data coincide well, but absolute values differ greatly, mainly caused by the limited spatial resolution of the measured data. Arzani et al. [ADES12] found 10% deviation of TKE (Section 6.3.2) obtained from 4D flow MRI and CFD simulations. Goubergrits et al. [GRY*15] found that systolic pressure drops (Section 6.3.1) can reliably be calculated using MRI-based CFD simulations. This could help to reduce the need for invasive catheterizations. Andersson et al. [ALEK15] underlined the value of MRI-based CFD simulations by studying TKE and flow eccentricity (Section 6.1.3) before and after treatment of aortic coarctation (a pathologic vessel narrowing).

8. Concluding Remarks

4D PC-MRI enables the measurement of 3D blood flow and its change over the heart cycle. Medical researchers start using these data to develop an increased understanding of healthy cardiovascular systems and to find indicators for the genesis and evolution of cardiovascular diseases. 4D PC-MRI is expected to significantly improve patient treatment, which was confirmed by recent medical studies [CRvdG*14,SAG*14]. A long-term goal is to obtain age- and gender-specific normative values for different flow parameters, which could help to refine current treatment guidelines. However, data in itself are not sufficient for significant medical progress. Until now, 4D PC-MRI is primarily used for research purposes, mainly, due to a lack of standardized and easy-to-use evaluation software with guided workflows and an automated report generation. Though, various free or commercial tools are being developed or were already established, such as:

- *FourFlow* by Heiberg et al. [HGT*12],
- *Bloodline* by Köhler et al. [KPG*15a],
- *Quantitative Flow Explorer* by Van Pelt et al. [VPBB*10],
- *MeVisFlow* by Hennemuth et al. [HFS*11],
- *GTFlow* by GyroTools,
- *QFlow ES* by Medis,
- *CMR 42* by Circle CVI,
- *Arterys*,
- *4D Flow Demonstrator* by Siemens [SCG*14],
- *EnSight* by CEI,
- an *OsiriX* plugin by Hüllebrand et al. [HHMK14],
- *VMTKLab* by Orobix and
- *Velomap* by Bock et al.

An overview of open visualization challenges was given by Van Pelt et al. [VPV13]. In this survey, we presented the state-of-the-art of quantitative and qualitative 4D PC-MRI data analysis and visualization to give future researchers in the field of cardiac 4D PC-MRI a strong starting point for further advancements, which may facilitate the evaluation of larger studies and make 4D PC-MRI viable for the clinical routine.

Abbreviations: **1D**: One-dimensional, **2D**: Two-dimensional, **3D**: Three-dimensional, **4D**: Four-dimensional, **A**: Anatomy image, B_0: Main magnetic field, **BFV**: Backward flow volume [ml], **BLAST**: Broad-use linear speed-up technique, **CFD**: Computational fluid dynamics, **CMR**: Cardiovascular magnetic resonance, **COM**: Center of mass, **CT**: Computerized tomography, **CVDs**: Cardiovascular diseases, **DOPRI5**(4): Dormand-Prince method, **DVM**: Differential velocity map, **DVR**: Direct volume rendering, **EVC**: Eigenvalue coherence, **FA**: Fourier analysis method, **FFV**: Forward flow volume [ml], **FTLE**: Finite-time Lyapunov exponents, **GAC**: Geodesic active contours, **GPU**: Graphics processing unit, **GRAPPA**: Generalized autocalibrating partially parallel acquisitions, **ISL**: Illuminated streamlines, **KE**: Kinetic energy, **LCS**: Lagrangian coherent structures, **LPC**: Local phase coherence, **M**: Magnitude image, **MIP**: Maximum intensity projection, **MR**: Magnetic resonance, **MRI**: Magnetic resonance imaging, **NFV**: Net flow volume [ml], **OIT**: Order-independent transparency, P: Measuring plane, **PBFV**: Percentaged Back Flow Volume, **PC**: Phase-contrast, **PCMRA**: Phase-contrast magnetic resonance angiography, **PPE**: Pressure Poisson equation, **PWV**: Pulse wave velocity, **RF**: Regurgitation fraction (%), **ROI**: Region of interest, S: Segmentation, **SENSE**: Sensitive encoding, **SNR**: Signal-to-noise ratio, **SV**: Stroke volume [ml], **TH**: Threshold method, **TKE**: Turbulent kinetic energy [J/m^3], **TMIP**: Temporal maximum intensity projection, **TTF**: Time-to-foot, **TTP**: Time-to-peak, **TTU**: Time-to-upstroke, **V**: Phase / Flow / Velocity image, **VAAS**: Vortex animations with adaptive speed, **VKE**: Ventricular kinetic energy, **VMTK**: The Vascular Modeling Toolkit, **VPM**: Vector pattern matching, **WSS**: Wall shear stress [Pa], **XCorr**: Cross-correlation, **x,y,z**: Spatial dimensions

Units: **g**: Grams, **kg**: Kilograms, **J**: Joule, **mJ**: Milliljoule, **m**: Meters, **mm**: Millimeters, **min**: Minutes, **ml**: Milliliters, **mmHg**: Millimeters of mercury, **Pa**: Pascal, **s**: Seconds, **ms**: Milliseconds, **T**: Tesla,

Math: **eig**: Function to calculate eigenvalues λ, J: Jacobian matrix, ℓ_1**-norm**: L_1 distance / taxicab geometry, N: Number, $\mathbb{R}$: Euclidean space, σ: Standard deviation,

Measures: E: Elastic (Young's) modulus, $\boldsymbol{fr}$: flow rate [ml/s], λ: Eigenvalue, d: Distance, λ_2: λ_2 vortex criterion, h: Wall thickness, H_d: Helicity density, H_r: Relative helicity, m: Mass, μ: Dynamic viscosity[Pa·s], $\vec{n}$: Normal vector, $\vec{p}_t$: 4D position at $\vec{p} \in \mathbb{R}^3$ and $t \in \mathbb{R}$, Δp: Pressure gradients, Q: Volumetric flow rate [m^3/s], r: Radius, p: Relative pressure [mmHg], ρ: Density [kg/m^3], $\dot{\gamma}$: Shear rate [1/s], $\vec{\tau}_{\mathbf{WSS}}$: Shear stress, t: Time [s], Δt: Time frame, T: Number of temporal positions, $\vec{v}$: Velocity vector [m/s], $||\vec{v}||$: Velocity (magnitude) [m/s], $\mathbf{V_{ENC}}$: Velocity encoding [m/s], $\vec{\omega}$: Vorticity, $||\vec{\omega}||$: Vorticity magnitude [1/s],

References

[ABT*95] ASMAR R., BENETOS A., TOPOUCHIAN J., LAURENT P., PANNIER B., BRISAC A. M., TARGET R., LEVY B. I.: Assessment of Arterial Distensibility by Automatic Pulse Wave Velocity Measurement. Validation and Clinical Application Studies. *Hypertension 26*, 3 (1995), 485–90. 15

[ADES12] ARZANI A., DYVERFELDT P., EBBERS T., SHADDEN S. C.: In Vivo Validation of Numerical Prediction for Turbulence Intensity in an Aortic Coarctation. *Annals of Biomedical Engineering 40*, 4 (2012), 860–70. 20

[AH11] ANGELELLI P., HAUSER H.: Straightening Tubular Flow for Side-by-Side Visualization. *IEEE Transactions on Visualization and Computer Graphics 17*, 12 (2011), 2063–70. 11

[AHGB09] AREVALILLO-HERRÁEZ M., GDEISAT M. A., BURTON D. R.: Hybrid Robust and Fast Algorithm for Three-dimensional Phase Unwrapping. *Applied Optics 48*, 32 (2009), 6313–23. 4

[AIR03] ANTIGA L., IORDACHE E. B., REMUZZI A.: Computational Geometry for Patient-Specific Reconstruction and Meshing of Blood Vessels from MR and CT Angiography. *IEEE Transactions on Medical Imaging 22*, 5 (2003), 674–84. 7

[ALEK15] ANDERSSON M., LANTZ J., EBBERS T., KARLSSON M.: Quantitative Assessment of Turbulence and Flow Eccentricity in an Aortic Coarctation: Impact of Virtual Interventions. *Cardiovascular Engineering and Technology 6*, 3 (2015), 281–93. 20

[ATY08] AKINS C. W., TRAVIS B., YOGANATHAN A. P.: Energy Loss for Evaluating Heart Valve Performance. *The Journal of Thoracic and Cardiovascular Surgery 136*, 4 (2008), 820–33. 18

[BB94] BOGREN H. G., BUONOCORE M. H.: Blood Flow Measurements in the Aorta and Major Arteries with MR Velocity Mapping. *Journal of Magnetic Resonance Imaging 4*, 2 (1994), 119–30. 13

[BBSS00] BOESE J. M., BOCK M., SCHOENBERG S. O., SCHAD L. R.: Estimation of Aortic Compliance Using Magnetic Resonance Pulse Wave Velocity Measurement. *Physics in Medicine and Biology 45*, 6 (2000), 1703–13. 15

[BCP*12] BRAMBILLA A., CARNECKY R., PEIKERT R., VIOLA I., HAUSER H.: Illustrative Flow Visualization: State of the Art, Trends and Challenges. In *Proceedings: Eurographics - State of the Art Reports* (Vienna, Austria, 2012), The Eurographics Association. 10

[BDV07] BIOUCAS-DIAS J. M., VALADÃO G.: Phase Unwrapping via Graph Cuts. *IEEE Transactions on Image Processing 16*, 3 (2007), 698–709. 4

[BEJE08] BAGHER-EBADIAN H., JIANG Q., EWING J. R.: A Modified Fourier-Based Phase Unwrapping Algorithm With an Application to MRI Venography. *Journal of Magnetic Resonance Imaging 27*, 3 (2008), 649–52. 4

[BFL*11] BOCK J., FRYDRYCHOWICZ A., LORENZ R., HIRTLER D., BARKER A. J., JOHNSON K. M., ARNOLD R., BURKHARDT H., HENNIG J., MARKL M.: In Vivo Noninvasive 4D Pressure Difference Mapping in the Human Aorta: Phantom Comparison and Application in Healthy Volunteers and Patients. *Journal of Magnetic Resonance Imaging 66*, 4 (2011), 1079–88. 18

[BFW*11] BIEGING E. T., FRYDRYCHOWICZ A., WENTLAND A. L., LANDGRAF B. R., JOHNSON K. M., WIEBEN O., FRANÇOIS C. J.: In Vivo Three-dimensional MR Wall Shear Stress Estimation in Ascending Aortic Dilatation. *Journal of Magnetic Resonance Imaging 33*, 3 (2011), 589–97. 17

[BGHK15] BINTER C., GÜLAN U., HOLZNER M., KOZERKE S.: On the Accuracy of Viscous and Turbulent Loss Quantification in Stenotic Aortic Flow Using Phase-Contrast MRI. *Journal of Magnetic Resonance in Medicine*, epub ahead of print (2015), 1–6. 18

[BH22] BRAMWELL J. C., HILL A. V.: The Velocity of the Pulse Wave in Man. *Proceedings of the Royal Society of London B: Biological Sciences 93*, 652 (1922), 298–306. 14

[BHB*13] BISSELL M. M., HESS A. T., BIASIOLLI L., GLAZE S. J., LOUDON M., PITCHER A., DAVIS A., PRENDERGAST B., MARKL M., BARKER A. J., NEUBAUER S., MYERSON S. G.: Aortic Dilation in Bicuspid Aortic Valve Disease: Flow Pattern Is a Major Contributor and Differs with Valve Fusion Type. *Circulation: Cardiovascular Imaging 6*, 4 (2013), 499–507. 2

[BHV99] BAKKER C. J., HOOGEVEEN R. M., VIERGEVER M. A.: Construction of a Protocol for Measuring Blood Flow by Two-Dimensional Phase-Contrast MRA. *Journal of Magnetic Resonance Imaging 9*, 1 (1999), 119–27. 3

[BK04] BOYKOV Y., KOLMOGOROV V.: An Experimental Comparison of Min-Cut/Max-Flow Algorithms for Energy Minimization in Vision. *IEEE Transactions on Pattern Analysis and Machine Intelligence 26*, 9 (2004), 1124–37. 7

[BKHM07] BOCK J., KREHER B., HENNING J., MARKL. M.: Optimized Pre-Processing of Time-Resolved 2D and 3D Phase Contrast MRI Data. In *Proceedings: International Society for Magnetic Resonance in Medicine* (Berlin, Germany, 2007), The International Society for Magnetic Resonance in Medicine, p. 3138. 4, 5

[BKM*13] BINTER C., KNOBLOCH V., MANKA R., SIGFRIDSSON A., KOZERKE S.: Bayesian Multipoint Velocity Encoding for Concurrent Flow and Turbulence Mapping. *Journal of Magnetic Resonance Imaging 69*, 5 (2013), 1337–45. 18

[BKP16] BEHRENDT B., KÖHLER B., PREIM B.: Enhancing Visibility of Blood Flow in Volume Rendered Cardiac 4D PC-MRI Data. In *Proceedings: Bildverarbeitung für die Medizin* (Berlin, Germany, 2016), Springer, p. to appear. 9

[BLAB15] BERGEN R. V., LIN H. Y., ALEXANDER M. E., BIDINOSTI C. P.: 4D MR Phase and Magnitude Segmentations with GPU Parallel Computing. *Journal of Magnetic Resonance Imaging 33*, 1 (2015), 134–45. 7

[BLV*15] BOSTAN E., LEFKIMMIATIS S., VARDOULIS O., STERGIOPULOS N., UNSER M.: Improved Variational Denoising of Flow Fields with Application to Phase-Contrast MRI Data. *IEEE Signal Processing Letters 22*, 6 (2015), 762–6. 6

[BMGS13] BORN S., MARKL M., GUTBERLET M., SCHEUERMANN G.: Illustrative Visualization of Cardiac and Aortic Blood Flow from 4D MRI Data. In *IEEE Pacific Visualization Symposium (PacificVis)* (Sydney, New South Wales, 2013), IEEE Computer Society, pp. 129–36. 11

[Boc12] BOCK J.: *Development and Testing of new Strategies for Pre-Processing and Analysis of 4D Flow-Sensitive MRI Data*. PhD thesis, Albert-Ludwigs-University, Freiburg, Germany, 2012. 5

[Bor14] BORN S.: *Illustrative Flow Visualization of 4D PC-MRI Blood Flow and CFD Data*. PhD thesis, University of Leipzig, Faculty of Mathematics and Computer Science, 2014. 10

[BPE*15] BUSTAMANTE M., PETERSSON S., ERIKSSON J., ALEHAGEN U., DYVERFELDT P., CARLHÄLL C. J., EBBERS T.: Atlas-based Analysis of 4D Flow CMR: Automated Vessel Segmentation and Flow Quan-

tification. *Journal of Cardiovascular Magnetic Resonance 17*, 1 (2015), Epub ahead of print. 7

[BPFL84] BRYANT D. J., PAYNE J. A., FIRMIN D. N., LONGMORE D. B.: Measurement of Flow with NMR Imaging Using a Gradient Pulse and Phase Difference Technique. *Journal of Computer Assisted Tomography 8*, 4 (1984), 588–93. 1

[BPM*13] BORN S., PFEIFLE M., MARKL M., GUTBERLET M., SCHEUERMANN G.: Visual Analysis of Cardiac 4D MRI Blood Flow Using Line Predicates. *IEEE Transactions on Visualization and Computer Graphics 19* (2013), 900–12. 1, 11

[BPS*13] BÄCHLER P., PINOCHET N., SOTELO J., CRELIER G., IRARRAZAVAL P., TEJOS C., URIBE S.: Assessment of Normal Flow Patterns in the Pulmonary Circulation by Using 4D Magnetic Resonance Velocity Mapping. *Journal of Magnetic Resonance Imaging 31*, 2 (2013), 178–88. 19

[BS94] BANKS D. C., SINGER B. A.: Vortex Tubes in Turbulent Flows: Identification, Representation, Reconstruction. In *Proceedings: IEEE Conference on Visualization (Vis)* (Washinton, District of Columbia, USA, 1994), IEEE Computer Society, pp. 132–9. 19

[BSK*14] BURRIS N. S., SIGOVAN M., KNAUER H. A., TSENG E. E., SALONER D., HOPE M. D.: Systolic Flow Displacement Correlates With Future Ascending Aortic Growth in Patients With Bicuspid Aortic Valves Undergoing Magnetic Resonance Surveillance. *Investigative Radiology 49*, 10 (2014), 635–9. 2, 16

[BT07] BORLAND D., TAYLOR R. M.: Rainbow Color Map (Still) Considered Harmful. *IEEE Computer Graphics and Applications 27*, 2 (2007), 14–7. 9

[Buo93] BUONOCORE M. H.: Blood Flow Measurement Using Variable Velocity Encoding in the RR Interval. *Journal of Magnetic Resonance in Medicine 29*, 6 (1993), 790–5. 3

[Buo98] BUONOCORE M. H.: Visualizing Blood Flow Patterns Using Streamlines, Arrows, and Particle Paths. *Journal of Magnetic Resonance in Medicine 40*, 2 (1998), 210–26. 10

[BvOB*14] BARKER A. J., VAN OOIJ P., BANDI K., GARCIA J., ALBAGHDADI M., MCCARTHY P., BONOW R. O., CARR J., COLLINS J., MALAISRIE S. C., MARKL M.: Viscous Energy Loss in the Presence of Abnormal Aortic Flow. *Journal of Magnetic Resonance in Medicine 72*, 3 (2014), 620–8. 18

[BVP*13] BOSTAN E., VARDOULIS O., PICCINI D., TAFTI P. D., STERGIOPULOS N., UNSER M.: Spatio-Temporal Regularization of Flow-Fields. In *Proceedings: IEEE International Symposium on Biomedical Imaging* (San Francisco, California, USA, 2013), IEEE Computer Society, pp. 824–7. 5

[BWJ*08] BOCK J., WIEBEN O., JOHNSON K., HENNIG J., MARKL M.: Optimal Processing to Derive Static PC-MRA From Time-Resolved 3D PC-MRI Data. In *Proceedings: International Society for Magnetic Resonance in Medicine* (Toronto, Ontario, Canada, 2008), The International Society for Magnetic Resonance in Medicine, p. 3053. 6

[BWK97] BHALERAO A., WESTIN C.-F., KIKINIS R.: Unwrapping Phase in 3D MR Phase Contrast Angiograms. In *Proceedings: First Joint Conference on Computer Vision, Virtual Reality and Robotics in Medicine and Medial Robotics and Computer-Assisted Surgery* (Grenoble, France, 1997), Springer, pp. 193–202. 4

[BZP*98] BERNSTEIN M. A., ZHOU X. J., POLZIN J. A., KING K. F., GANIN A., PELC N. J., GLOVER G. H.: Concomitant Gradient Terms in Phase Contrast MR: Analysis and Correction. *Journal of Magnetic Resonance in Medicine 39*, 2 (1998), 300–8. 4, 5

[CBW*14] CARNECKY R., BRUNNER T. BORN S., WASER J., HEINE C., PEIKERT R.: Vortex Detection in 4D MRI Data: Using the Proper Orthogonal Decomposition for Improved Noise-Robustness. In *Proceedings: Eurographics Conference on Visualization (EuroVis) - Short Papers* (Swansea, UK, 2014), The Eurographics Association, pp. 127–31. 12

[CHTA12] CARLSSON M., HEIBERG E., TÖGER J., ARHEDEN H.: Quantification of Left and Right Ventricular Kinetic Energy Using Four-Dimensional Intracardiac Magnetic Resonance Imaging Flow Measurements. *American Journal of Physiology - Heart and Circulatory Physiology 302*, 4 (2012), H893–H900. 18

[Cla76] CLARK C.: Turbulent Velocity Measurements in a Model of Aortic Stenosis. *Journal of Biomechanics 9*, 11 (1976), 677–87. 18

[CNS04] CHUNG A. C. S., NOBLE J. A., SUMMERS P.: Vascular Segmentation of Phase Contrast Magnetic Resonance Angiograms Based on Statistical Mixture Modeling and Local Phase Coherence. *IEEE Transactions on Medical Imaging 23*, 12 (2004), 1490–507. 6

[CP02] CUSACK R., PAPADAKIS N.: New Robust 3-D Phase Unwrapping Algorithms: Application to Magnetic Field Mapping and Undistorting Echoplanar Images. *Neuroimage 16*, 3 (2002), 754–64. 4

[CPT02] CHENG C. P., PARKER D., TAYLOR C. A.: Quantification of Wall Shear Stress in Large Blood Vessels Using Lagrangian Interpolation Functions With Cine Phase-contrast Magnetic Resonance Imaging. *Annals of Biomedical Engineering 30*, 8 (2002), 1020–32. 17

[CRK*14] CALKOEN E. E., ROEST A., KROFT L. J., VAN DEN BOOGAARD P. J., JONGBLOED M. R., VAN DER GEEST R. J., DE ROOS A., WESTENBERG J. J.: The Added Value of Streamline Visualization in the Evaluation of Left Atrioventricular Valve Flow and Left Ventricular Diastolic Function with 4DFlow MRI. *Journal of Cardiovascular Magnetic Resonance 16*, Suppl 1 (2014), P353. 10

[CRvdG*14] CALKOEN E. E., ROEST A. A. W., VAN DER GEEST R. J., DE ROOS A., WESTENBERG J. J. M.: Cardiovascular Function and Flow by 4-Dimensional Magnetic Resonance Imaging Techniques: New Applications. *Journal of Thoracic Imaging 29*, 3 (2014), 185–96. 2, 20

[CSCW07] CHERNOBELSKY A., SHUBAYEV O., COMEAU C. R., WOLFF S. D.: Baseline Correction of Phase Contrast Images Improves Quantification of Blood Flow in the Great Vessels. *Journal of Cardiovascular Magnetic Resonance 9*, 4 (2007), 681–5. 4, 5

[DBB*15] DYVERFELDT P., BISSELL M., BARKER A. J., BOLGER A. F., CARLHÄLL C.-J., EBBERS T., FRANÇOIS C. J., FRYDRYCHOWICZ A., GEIGER J., GIESE D., HOPE M. D., KILNER P. J., KOZERKE S., MYERSON S., NEUBAUER S., WIEBEN O., MARKL M.: 4D Flow Cardiovascular Magnetic Resonance Consensus Statement. *Journal of Cardiovascular Magnetic Resonance 17*, 1 (2015), 1–19. 2

[DEL14] DYVERFELDT P., EBBERS T., LÄNNE T.: Pulse Wave Velocity With 4D Flow MRI: Systematic Differences and Age-related Regional Vascular Stiffness. *Journal of Magnetic Resonance Imaging 32*, 10 (2014), 1266–71. 14, 15

[DFS*15] DONATI F., FIGUEROA C. A., SMITH N. P., LAMATA P., NORDSLETTEN D. A.: Non-invasive Pressure Difference Estimation from PC-MRI Using the Work-Energy Equation. *Medical Image Analysis 26*, 1 (2015), 159–72. 18

[dHvPJV14] DE HOON N., VAN PELT R. F. P., JALBA A., VILANOVA A.: 4D MRI Flow Coupled to Physics-Based Fluid Simulation for Blood-Flow Visualization. *Computer Graphics Forum 33*, 3 (2014), 121–30. 20

[DKM*13] DREXL J., KHAN H., MARKL M., HENNEMUTH A., MEIER S., LORENZ R., HAHN H. K.: Detection of Vortical Structures in 4D Velocity Encoded Phase Contrast MRI Data Using Vector Template Matching. In *Proceedings: Functional Imaging and Modeling of the Heart*. 2013, pp. 276–83. 12, 15

[DKS*08] DYVERFELDT P., KVITTING J.-P. E., SIGFRIDSSON A., ENGVALL J., BOLGER A. F., EBBERS T.: Assessment of Fluctuating Velocities in Disturbed Cardiovascular Blood Flow: In Vivo Feasibility of Generalized Phase-Contrast MRI. *Journal of Magnetic Resonance Imaging 28*, 3 (2008), 655–63. 18

[DNSL14] DONATI F., NORDSLETTEN D. A., SMITH N. P., LAMATA P.: Pressure Mapping from Flow Imaging: Enhancing Computation of the Viscous Term Through Velocity Reconstruction in Near-Wall Regions. In *Proceedings: 36th Annual International Conference of the IEEE Engineering in Medicine and Biology Society* (Chicago, Illinois, USA, 2014), IEEE Computer Society, pp. 5097–100. 18

[DP80] DORMAND J. R., PRINCE P. J.: A Family of Embedded Runge-Kutta Formulae. *Journal of Computational and Applied Mathematics 6*, 1 (1980), 19–26. 10

[DRL*11] DOGUI A., REDHEUIL A., LEFORT M., DECESARE A., KACHENOURA N., HERMENT A., MOUSSEAUX E.: Measurement of Aortic Arch Pulse Wave Velocity in Cardiovascular MR: Comparison of Transit Time Estimators and Description of a New Approach. *Journal of Magnetic Resonance Imaging 33*, 6 (2011), 1321–9. 15

[DSKE06] DYVERFELDT P., SIGFRIDSSON A., KVITTING J.-P. E., EBBERS T.: Quantification of Intravoxel Velocity Standard Deviation and Turbulence Intensity by Generalizing Phase-contrast MRI. *Journal of Magnetic Resonance in Medicine 56*, 4 (2006), 850–8. 18

[Ebb11] EBBERS T.: Flow Imaging: Cardiac Applications of 3D Cine Phase-Contrast MRI. *Current Cardiovascular Imaging Reports 4*, 2 (2011), 127–33. 2

[EBRI09] EVERTS M. H., BEKKER H., ROERDINK J. B. T. M., ISENBERG T.: Depth-Dependent Halos: Illustrative Rendering of Dense Line Data. *IEEE Transactions on Visualization and Computer Graphics 15*, 6 (2009), 1299–306. 10

[EBRI15] EVERTS M. H., BEKKER H., ROERDINK J. B. T. M., ISENBERG T.: Interactive Illustrative Line Styles and Line Style Transfer Functions for Flow Visualization. *Computing Research Repository* (2015). 10

[ECW*14] ELBAZ M. S. M., CALKOEN E. E., WESTENBERG J. J. M., LELIEVELDT B. P. F., ROEST A. A. W., VAN DER GEEST R. J.: Vortex Flow During Early and Late Left Ventricular Filling in Normal Subjects: Quantitative Characterization Using Retrospectively-gated 4D Flow Cardiovascular Magnetic Resonance and Three-Dimensional Vortex Core Analysis. *Journal of Cardiovascular Magnetic Resonance 16*, 78 (2014), 12. 12

[EF09] EBBERS T., FARNEBÄCK G.: Improving Computation of Cardiovascular Relative Pressure Fields from Velocity MRI. *Journal of Magnetic Resonance Imaging 30*, 1 (2009), 54–61. 18

[ELvdG15] ELBAZ M. S. M., LELIEVELDT B. P. F., VAN DER GEEST R. J.: Hierarchical Shape Distributions for Automatic Identification of 3D Diastolic Vortex Rings from 4D Flow MRI. In *Proceedings: Medical Image Computing and Computer-Assisted Intervention* (Munich, Germany, 2015), Springer, pp. 467–75. 12

[EWB*01] EBBERS T., WIGSTRÖM L., BOLGER A. F., ENGVALL J., KARLSSON M.: Estimation of Relative Cardiovascular Pressures Using Time-resolved Three-dimensional Phase Contrast MRI. *Journal of Magnetic Resonance in Medicine 45*, 5 (2001), 872–9. 17

[FCL09] FORSBERG A. S., CHEN J., LAIDLAW D. H.: Comparing 3D Vector Field Visualization Methods: A User Study. *IEEE Transactions on Visualization and Computer Graphics 15*, 6 (2009), 1219–26. 10

[FFJH*08] FIELDEN S. W., FORNWALT B. K., JEROSCH-HEROLD M.,

EISNER R. L., STILLMAN A. E., OSHINSKI J. N.: A New Method for the Determination of Aortic Pulse Wave Velocity Using Cross-Correlation on 2D PCMR Velocity Data. *Journal of Magnetic Resonance Imaging 27*, 6 (2008), 1382–7. 15

[FGG*13] FAIR M., GATEHOUSE P. D., GREISER A., DRIVAS P., FIRMIN D. N.: A Novel Approach to Phase-Contrast Velocity Offset Correction by In Vivo High-SNR Acquisitions. *Journal of Cardiovascular Magnetic Resonance 15*, Suppl 1 (2013), P56. 5

[FHH*10] FRIMAN O., HENNEMUTH A., HARLOFF A., BOCK J., MARKL M., PEITGEN H.-O.: Probabilistic 4D Blood Flow Mapping. In *Proceedings: Medical Image Computing and Computer Assisted Intervention* (Beijing, China, 2010), Springer, pp. 416–23. 20

[GBvO*15] GUZZARDI D. G., BARKER A. J., VAN OOIJ P., MALAISRIE S. C., PUTHUMANA J. J., BELKE D. D., MEWHORT H. E., SVYSTONYUK D. A., KANG S., VERMA S., COLLINS J., CARR J., BONOW R. O., MARKL M., THOMAS J. D., MCCARTHY P. M., FEDAK P. W.: Valve-Related Hemodynamics Mediate Human Bicuspid Aortopathy: Insights From Wall Shear Stress Mapping. *Journal of the American College of Cardiology 66*, 8 (2015), 892–900. 2

[Gib98] GIBSON S. F. F.: Constrained Elastic Surface Nets: Generating Smooth Surfaces from Binary Segmented Data. In *Proceedings: Conference on Medical Image Computing and Computer-Assisted Intervention* (Cambridge, Massachusetts, USA, 1998), Springer, pp. 888–98. 8

[GJH*02] GRISWOLD M. A., JAKOB P. M., HEIDEMANN R. M., NITTKA M., JELLUS V., WANG J., KIEFER B., HAASE A.: Generalized Autocalibrating Partially Parallel Acquisitions (GRAPPA). *Journal of Magnetic Resonance in Medicine 47*, 6 (2002), 1202–10. 3

[GLvP*12] GASTEIGER R., LEHMANN D. J., VAN PELT R. F. P., JANIGA G., BEUING O., VILANOVA A., THEISEL H., PREIM B.: Automatic Detection and Visualization of Qualitative Hemodynamic Characteristics in Cerebral Aneurysms. *IEEE Transactions on Visualization and Computer Graphics 18*, 12 (2012), 2178–87. 1, 11

[GMK*14] GOEL A., MCCOLL R., KING K. S., WHITTEMORE A., PESHOCK R. M.: Fully Automated Tool to Identify the Aorta and Compute Flow Using Phase-Contrast MRI: Validation and Application in a Large Population Based Study. *Journal of Magnetic Resonance Imaging 40*, 1 (2014), 221–8. 8

[GNBP11] GASTEIGER R., NEUGEBAUER M., BEUING O., PREIM B.: The FLOWLENS: A Focus-and-Context Visualization Approach for Exploration of Blood Flow in Cerebral Aneurysms. *IEEE Transactions on Visualization and Computer Graphics 17*, 12 (2011), 2183–92. 1

[GNKP10] GASTEIGER R., NEUGEBAUER M., KUBISCH C., PREIM B.: Adapted Surface Visualization of Cerebral Aneurysms with Embedded Blood Flow Information. In *Proceedings: Eurographics Workshop on Visual Computing for Biology and Medicine* (Leipzig, Germany, 2010), The Eurographics Association, pp. 25–32. 8

[GRY*15] GOUBERGRITS L., RIESENKAMPFF E., YEVTUSHENKO P., SCHALLER J., KERTZSCHER U., HENNEMUTH A., BERGER F., SCHUBERT S., KUEHNE T.: MRI-based Computational Fluid Dynamics for Diagnosis and Treatment Prediction: Clinical Validation Study in Patients with Coarctation of Aorta. *Journal of Magnetic Resonance Imaging 41*, 4 (2015), 909–16. 20

[GT10] GÜLSÜN M. A., TEK H.: Segmentation of Carotid Arteries by Graph-Cuts Using Centerline Models. In *Proceedings: International Society for Optics and Photonics (SPIE)* (San Diego, California, 2010), SPIE, p. 762530. 7

[HBG*13] HESS A. T., BISSELL M. M., GLAZE S. J., PITCHER A., MYERSON S., NEUBAUER S., ROBSON M. D.: Evaluation of Circulation, Γ, as a Quantifying Metric in 4D Flow MRI. *Journal of Cardiovascular Magnetic Resonance 15*, Suppl 1 (2013), E36. 19

[HBN*15] HESS A. T., BISSELL M. M., NTUSI N. A. B., LEWIS A. J. M., TUNNICLIFFE E. M., GREISER A., STALDER A. F., FRANCIS J. M., MYERSON S. G., NEUBAUER S., ROBSON M. D.: Aortic 4D Flow: Quantification of Signal-to-Noise Ratio as a Function of Field Strength and Contrast Enhancement for 1.5T, 3T, and 7T. *Journal of Magnetic Resonance in Medicine 73*, 5 (2015), 1864–71. 3

[HBTA78] HATLE L., BRUBAKK A., TROMSDAL A., ANGELSEN B.: Noninvasive Assessment of Pressure Drop in Mitral Stenosis by Doppler Ultrasound. *British Heart Journal 40*, 2 (1978), 131–40. 17

[HBV99] HOOGEVEEN R. M., BAKKER C. J., VIERGEVER M. A.: MR Phase-Contrast Flow Measurement with Limited Spatial Resolution in Small Vessels: Value of Model-based Image Analysis. *Journal of Magnetic Resonance Imaging 41*, 3 (1999), 520–8. 14

[HEWK03] HEIBERG E., EBBERS T., WIGSTRÖM L., KARLSSON M.: Three-Dimensional Flow Characterization Using Vector Pattern Matching. *IEEE Transactions on Visualization and Computer Graphics 9*, 3 (2003), 313–9. 12, 13

[HFS*11] HENNEMUTH A., FRIMAN O., SCHUMANN C., BOCK J., DREXL J., HUELLEBRAND M., MARKL M., PEITGEN H.-O.: Fast Interactive Exploration of 4D MRI Flow Data. In *Proceedings: International Society for Optics and Photonics (SPIE)* (Lake Buena Vista, Florida, 2011), SPIE, pp. 79640E–11. 6, 7, 11, 20

[HGT*12] HEIBERG E., GREEN C., TÖGER J., ANDERSSON A. M., CARLSSON M., ARHEDEN H.: FourFlow - Open Source Code Software for Quantification and Visualization of Time-Resolved Three-Directional Phase Contrast Magnetic Resonance Velocity Mapping. *Journal of Cardiovascular Magnetic Resonance 14*, Suppl 1 (2012), W14. 20

[HH08] HOPE T. A., HERFKENS R. J.: Imaging of the Thoracic Aorta with Time-Resolved Three-Dimensional Phase-Contrast MRI: A Review. *The Journal of Thoracic and Cardiovascular Surgery 20*, 4 (2008), 358–64. 2

[HHM*10] HOPE M. D., HOPE T. A., MEADOWS A. K., ORDOVAS K. G., URBANIA T. H., ALLEY M. T., HIGGINS C. B.: Bicuspid Aortic Valve: Four-dimensional MR Evaluation of Ascending Aortic Systolic Flow Patterns. *Radiology 255*, 1 (2010), 53–61. 12

[HHMK14] HÜLLEBRAND M., HENNEMUTH A., MESSROGHLI D., KÜHNE T.: An OsiriX Plugin for Integrated Cardiac Image Processing Research. In *Proceedings: International Society for Optics and Photonics (SPIE)* (San Diego, California, USA, 2014), SPIE, p. 90390D. 20

[HMW*07] HOPE T. A., MARKL M., WIGSTRÖM L., ALLEY M. T., MILLER D. C., HERFKENS R. J.: Comparison of Flow Patterns in Ascending Aortic Aneurysms and Volunteers Using Four-dimensional Magnetic Resonance Velocity Mapping. *Journal of Magnetic Resonance Imaging 26*, 6 (2007), 1471–9. 12

[HSD13] HOPE M. D., SEDLIC T., DYVERFELDT P.: Cardiothoracic Magnetic Resonance Flow Imaging. *Journal of Thoracic Imaging 28*, 4 (2013), 217–30. 2, 13, 14

[HSU*10] HEIBERG E., SJÖGREN J., UGANDER M., CARLSSON M., ENGBLOM H., ARHEDEN H.: Design and Validation of Segment - Freely Available Software for Cardiovascular Image Analysis. *BioMedCentral (BMC) Medical Imaging 10*, 1 (2010). 9

[IG97] INTERRANTE V., GROSCH C.: Strategies for Effectively Visualizing 3D Flow with Volume LIC. In *Proceedings: IEEE Conference on Visualization (Vis)* (Phoenix, Arizona, USA, 1997), IEEE Computer Society, pp. 421–4. 10

[ISG*12] ITU L. M., SHARMA1 P., GÜLSÜN M. A., MIHALEF V., KAMEN A., GREISER A.: Determination of Time-varying Pressure Field from Phase Contrast MRI Data. *Journal of Cardiovascular Magnetic Resonance 14*, Suppl 1 (2012), W36. 18

[Jen03] JENKINSON M.: Fast, Automated, N-dimensional Phase-unwrapping Algorithm. *Journal of Magnetic Resonance in Medicine 49*, 1 (2003), 193–7. 4

[JH95] JEONG J., HUSSAIN F.: On the Identification of a Vortex. *Journal of Fluid Mechanics 285* (1995), 69–94. 12

[JMT05] JIANG M., MACHIRAJU R., THOMPSON D.: Detection and Visualization of Vortices. In *The Visualization Handbook* (Orlando, Florida, USA, 2005), Academic Press, Inc., pp. 295–309. 12

[JSH12] JAMRIŠKA O., SÝKORA D., HORNUNG A.: Cache-Efficient Graph Cuts on Structured Grids. In *Proceedings: IEEE Conference on Computer Vision and Pattern Recognition* (Providence, Rhode Island, USA, 2012), IEEE Computer Society, pp. 3673–80. 7

[KBvP*15] KÖHLER B., BORN S., VAN PELT R. F. P., PREIM U., PREIM B.: A Survey of Cardiac 4D PC-MRI Data Processing. In *Proceedings: Eurographics Workshop on Visual Computing for Biology and Medicine* (Chester, UK, 2015), The Eurographics Association, p. to appear. 2

[KFU*87] KLIPSTEIN R. H., FIRMIN D. N., UNDERWOOD S. R., REES R. S., LONGMORE D. B.: Blood Flow Patterns in the Human Aorta Studied by Magnetic Resonance. *British Heart Journal 58*, 4 (1987), 316–23. 1, 13

[KGG*12] KRISHNAN H., GARTH C., GÜHRING J., GÜLSÜN M. A., GREISER A., JOY K. I.: Analysis of Time-Dependent Flow-Sensitive PC-MRI Data. *IEEE Transactions on Visualization and Computer Graphics 18*, 6 (2012), 966–77. 19

[KGP*13] KÖHLER B., GASTEIGER R., PREIM U., THEISEL H., GUTBERLET M., PREIM B.: Semi-Automatic Vortex Extraction in 4D PC-MRI Cardiac Blood Flow Data Using Line Predicates. *IEEE Transactions on Visualization and Computer Graphics 19*, 12 (2013), 2773–82. 1, 10, 12

[KKB*15] KARI F. A., KOCHER N., BEYERSDORF F., TSCHEUSCHLER A., MEFFERT P., RYLSKI B., SIEPE M., RUSSE M. F., HOPE M. D.: Four-dimensional Magnetic Resonance Imaging-derived Ascending Aortic Flow Eccentricity and Flow Compression are Linked to Aneurysm Morphology. *Interactive Cardiovascular and Thoracic Surgery 20*, 5 (2015), 582–7. 16

[KLM*12] KRITTIAN S. B. S., LAMATA P., MICHLER C., NORDSLETTEN D. A., BOCK J., BRADLEY C. P., PITCHER A., KILNER P. J., MARKL M., SMITH N. P.: A Finite-element Approach to the Direct Computation of Relative Cardiovascular Pressure from Time-resolved MR Velocity Data. *Medical Image Analysis 16*, 5 (2012), 1029–37. 18

[KMP*15] KÖHLER B., MEUSCHKE M., PREIM U., FISCHBACH K., GUTBERLET M., PREIM B.: Two-Dimensional Plot Visualization of Aortic Vortex Flow in Cardiac 4D PC-MRI Data. In *Proceedings: Bildverarbeitung für die Medizin* (Lübeck, Germany, 2015), Springer, pp. 257–61. 12

[KMR*01] KÖHLER U., MARSHALL I., ROBERTSON M. B., LONG Q., XU X. Y., HOSKINS P. R.: MRI Measurement of Wall Shear Stress Vectors in Bifurcation Models and Comparison With CFD Predictions. *Journal of Magnetic Resonance Imaging 14*, 5 (2001), 563–73. 17

[KPG*15a] KÖHLER B., PREIM U., GROTHOFF M., GUTBERLET M., FISCHBACH K., PREIM B.: Guided Analysis of Cardiac 4D PC-MRI Blood Flow Data. In *Proceedings: Eurographics Short Papers and Medical Prize Awards* (Zürich, Switzerland, 2015), The Eurographics Association, p. to appear. 20

[KPG*15b] KÖHLER B., PREIM U., GROTHOFF M., GUTBERLET M., FISCHBACH K., PREIM B.: Motion-aware Stroke Volume Quantification in 4D PC-MRI Data of the Human Aorta. *International Journal for Computer Assisted Radiology and Surgery 11*, 2 (2015), 169–79. 7, 9

[KPG*15c] KÖHLER B., PREIM U., GROTHOFF M., GUTBERLET M., FISCHBACH K., PREIM B.: Robust Cardiac Function Assessment in 4D PC-MRI Data of the Aorta and Pulmonary Artery. *Computer Graphics Forum*, Epub ahead of print (2015). 7, 14, 15

[KPG*16] KÖHLER B., PREIM U., GROTHOFF M., GUTBERLET M., PREIM B.: Adaptive Animations of Vortex Flow Extracted from Cardiac 4D PC-MRI Data. In *Proceedings: Bildverarbeitung für die Medizin* (Berlin, Germany, 2016), Springer, p. to appear. 11

[KW03] KRÜGER J., WESTERMANN R.: Acceleration Techniques for GPU-based Volume Rendering. In *Proceedings: IEEE Conference on Visualization (Vis)* (Seattle, Washington, USA, 2003), IEEE Computer Society. 9

[LABFL09] LESAGE D., ANGELINI E. D., BLOCH I., FUNKA-LEA G.: A Review of 3D Vessel Lumen Segmentation Techniques: Models, Features and Extraction Schemes. *Medical Image Analysis 13*, 6 (2009), 819–45. 6

[LAW*14] LI W., AVRAM A. V., WU B., XIAO X., LIU C.: Integrated Laplacian-based Phase Unwrapping and Background Phase Removal for Quantitative Susceptibility Mapping. *NMR in Biomedicine 27*, 2 (2014), 219–27. 4

[LBB*14] LORENZ R., BOCK J., BARKER A. J., VON KNOBELSDORFF-BRENKENHOFF F., WALLIS W., KORVINK J. G., BISSELL M. M., SCHULZ-MENGER J., MARKL M.: 4D Flow Magnetic Resonance Imaging in Bicuspid Aortic Valve Disease Demonstrates Altered Distribution of Aortic Blood Flow Helicity . *Journal of Magnetic Resonance in Medicine 71*, 4 (2014), 1542–53. 2, 19

[LBS*14] LORENZ R., BOCK J., SNYDER J., KORVINK J. G., JUNG B. A., MARKL M.: Influence of Eddy Current, Maxwell and Gradient Field Corrections on 3D Flow Visualization of 3D CINE PC-MRI Data. *Journal of Magnetic Resonance in Medicine 72*, 33 (2014), 33–40. 4, 5

[LC87] LORENSEN W. E., CLINE H. E.: Marching Cubes: A High Resolution 3D Surface Construction Algorithm. *SIGGRAPH Computer Graphics 21*, 4 (1987), 163–9. 8

[LDE14] LANTZ J., DYVERFELDT P., EBBERS T.: Improving Blood Flow Simulations by Incorporating Measured Subject-Specific Wall Motion. *Cardiovascular Engineering and Technology 5*, 3 (2014), 261–9. 9

[LFN*86] LONGMORE D. B., FIRMIN D. N., NAYLER G. L., UNDERWOOD S. R., KLIPSTEIN R. H.: Cine Magnetic Resonance Blood Flow Imaging in Clinical Use. *JMRI 4*, 2 (1986), 157. 1

[LGK12] LANTZ J., GÅRDHAGEN R., KARLSSON M.: Quantifying Turbulent Wall Shear Stress in a Subject Specific Human Aorta Using Large Eddy Simulation. *Medical Engineering & Physics 34*, 8 (2012), 1139–48. 20

[LGP14] LAWONN K., GASTEIGER R., PREIM B.: Adaptive Surface Visualization of Vessels With Animated Blood Flow. *Computer Graphics Forum 33*, 8 (2014), 16–27. 8

[LHKS88] LATSON T. W., HUNTER W. C., KATOH N., SAGAWA K.: Effect of Nitroglycerin on Aortic Impedance, Diameter, and Pulse-wave Velocity. *Circulation Research 62*, 5 (1988), 884–90. 15

[LHM*05] LANKHAAR J.-W., HOFMAN M. B. M., MARCUS J. T., ZWANENBURG J. J. M., FAES T. J. C., VONK-NOORDEGRAAF A.: Correction of Phase Offset Errors in Main Pulmonary Artery Flow Quantification. *Journal of Magnetic Resonance Imaging 22*, 1 (2005), 73–9. 5

[LJLW11] LOECHER M., JOHNSON K., LANDGRAF B., WIEBEN O.: 4D Gradient Based Phase Unwrapping for PC-MR Flow Data. In *Proceedings: International Society for Magnetic Resonance in Medicine* (Montréal, Québec, Canada, 2011), The International Society for Magnetic Resonance in Medicine, p. 3284. 4

[LKJ*05] LAIDLAW D. H., KIRBY R. M., JACKSON C. D., DAVIDSON J. S., MILLER T. S., DA SILVA M., WARREN W. H., TARR M. J.: Comparing 2D Vector Field Visualization Methods: A User Study. *IEEE Transactions on Visualization and Computer Graphics 11*, 1 (2005), 59–70. 9

[LKN*14] LAMATA P. AND P. A., KRITTIAN S., NORDSLETTEN D., BISSELL M. M., CASSAR T., BARKER A. J., MARKL M., NEUBAUER S., SMITH N. P.: Aortic Relative Pressure Components Derived from Four-dimensional Flow Cardiovascular Magnetic Resonance. *Journal of Magnetic Resonance Imaging 72*, 4 (2014), 1162–9. 18

[LKTW12] LOECHER M., KECSKEMETI S., TURSKI P., WIEBEN O.: Comparison of Divergence-free Algorithms for 3D MRI With Three-directional Velocity Encoding. *Journal of Cardiovascular Magnetic Resonance 14*, Suppl 1 (2012), W64. 5

[LMLG02] LOTZ J., MEIER C., LEPPERT A., GALANSKI M.: Cardiovascular Flow Measurement with Phase-Contrast MR Imaging: Basic Facts and Implementation. *Radiographics 22*, 3 (2002), 651–71. 2, 3, 5

[LS10] LIU J., SUN J.: Parallel Graph-Cuts by Adaptive Bottom-Up Merging. In *Proceedings: IEEE Conference on Computer Vision and Pattern Recognition* (San Francisco, California, USA, 2010), IEEE Computer Society, pp. 2181–8. 7

[LSJW15] LOECHER M., SCHRAUBEN E., JOHNSON K. M., WIEBEN O.: Phase Unwrapping in 4D MR Flow With a 4D Single-Step Laplacian Algorithm. *Journal of Magnetic Resonance Imaging* (2015), Epub ahead of print. 4

[MAI99] MALEK A. M., ALPER S. L., IZUMO S.: Hemodynamic Shear Stress and its Role in Atherosclerosis. *The Journal of the Americal Medical Association 282*, 21 (1999), 2035–42. 16

[Mar05] MARKL M.: Velocity Encoding and Flow Imaging, 2005. 3

[MBA*03] MARKL M., BAMMER R., ALLEY M. T., ELKINS C. J., DRANEY M. T., BARNETT A., MOSELEY M. E., GLOVER G. H., PELC N. J.: Generalized Reconstruction of Phase Contrast MRI: Analysis and Correction of the Effect of Gradient Field Distortions. *Journal of Magnetic Resonance in Medicine 50*, 4 (2003), 791–801. 4, 5

[McD68] MCDONALD D. A.: Regional Pulse-wave Velocity in the Arterial Tree. *Journal of Applied Physiology 24*, 1 (1968), 73–8. 14

[MDHH13] MIRZAEE H., DREXL J., HENNEMUTH A., HARLOFF A.: Investigation of Arterial Pulse Wave Velocity Based on 4D Phase Contrast MR Flow Imaging (4D PC MRI). In *Proceedings: Radiological Society of North America 2013 Scientific Assembly and Annual Meeting* (Chicago, Illinois, USA, 2013). 15

[MFK*12] MARKL M., FRYDRYCHOWICZ A., KOZERKE S., HOPE M. D., WIEBEN O.: 4D Flow MRI. *Journal of Magnetic Resonance Imaging 36*, 5 (2012), 1015–36. 3

[MFU*99] MASARYK A. M., FRAYNE R., UNAL O., KRUPINSKI E., STROTHER C. M.: In Vitro and in Vivo Comparison of Three MR Measurement Methods for Calculating Vascular Shear Stress in the Internal Carotid Artery. *American Journal of Neuroradiology 20*, 2 (1999), 237–45. 16

[MH15] MIRZAEE H., HENNEMUTH A.: Noninvasive Measurement of Intravascular Pressure Gradients Based on 3D Anatomy and 4D Flow Image Fusion. In *Proceedings: International Society for Magnetic Resonance in Medicine* (Toronto, Ontario, Canada, 2015), The International Society for Magnetic Resonance in Medicine, p. 2753. 6

[MHD*13] MEIER S., HENNEMUTH A., DREXL J., BOCK J., JUNG B., PREUSSER T.: A Fast and Noise-Robust Method for Computation of Intravascular Pressure Difference Maps from 4D PC-MRI Data. In *Proceedings: Statistical Atlases and Computational Models of the Heart. Imaging and Modelling Challenges (STACOM)* (Nice, France, 2013), Springer, pp. 215–24. 6, 18

[MHF*10] MEIER S., HENNEMUTH A., FRIMAN O., BOCK J., MARKL M., PREUSSER T.: Non-invasive 4D Blood Flow and Pressure Quantification in Central Blood Vessels via PC-MRI. In *Proceedings: Computing in Cardiology Conference (CinC)* (Belfast, Northern Ireland, 2010), IEEE Computer Society, pp. 903–6. 18

[MKE11] MARKL M., KILNER P. J., EBBERS T.: Comprehensive 4D Velocity Mapping of the Heart and Great Vessels by Cardiovascular Magnetic Resonance. *Journal of Cardiovascular Magnetic Resonance 13*, 7 (2011). 2

[ML89] MOHIADDIN R. H., LONGMORE D. B.: MRI Studies of Atherosclerotic Vascular Disease: Structural Evaluation and Physiological Measurements. *British Medical Bulletin 45*, 4 (1989), 968–90. 14

[MLK*16] MEUSCHKE M., LAWONN K., KÖHLER B., PREIM U., PREIM B.: Clustering of Aortic Vortex Flow in Cardiac 4D PC-MRI Data. In *Proceedings: Bildverarbeitung für die Medizin* (Berlin, Germany, 2016), Springer, p. to appear. 12

[MLP*10] MCLOUGHLIN T., LARAMEE R. S., PEIKERT R., POST F. H., CHEN M.: Over Two Decades of Integration-Based, Geometric Flow. *Computer Graphics Forum 29*, 6 (2010), 1807–29. 10

[MMS*14] MAGRATH P., MARKL M., STALDER A. F., GÜLSÜN M. A., SPOTTISWOODE B.: Improved Semi-automated Pulse Wave Velocity Analysis in the Thoracic Aorta Using 4D Flow MRI. In *Proceedings: International Society for Magnetic Resonance in Medicine* (Milan, Italy, 2014), The International Society for Magnetic Resonance in Medicine, p. 2482. 15

[MPR*09] MORBIDUCCI U., PONZINI R., RIZZO G., CADIOLI M., ESPOSITO A., DE COBELLI F., DEL MASCHIO A., MONTEVECCHI F. M., REDAELLI A.: In Vivo Quantification of Helical Blood Flow in Human Aorta by Time-resolved Three-dimensional Cine Phase Contrast Magnetic Resonance Imaging. *Annals of Biomedical Engineering 37*, 3 (2009), 516–31. 19

[MR93] MOHIADDIN RH1 FIRMIN DN L. D.: Age-related changes of human aortic flow wave velocity measured noninvasively by magnetic resonance imaging. *Journal of Applied Physiology (1985) 74*, 1 (1993), 492–7. 15

[MRG*14] MIHALEF V., RAPAKA S., GÜLSÜN M. A., SCORZA A., SHARMA P., ITU L. M., KAMEN A., BARKER A. J., MARKL M., COMANICIU D.: Model-Based Estimation of 4D Relative Pressure Map from 4D Flow MR Images. In *Proceedings: Statistical Atlases and Computational Models of the Heart. Imaging and Modelling Challenges (STACOM)* (Nagoya, Japan, 2014), Springer, pp. 236–43. 18

[MSB14] MARKL M., S. S., BARKER A. J.: 4D Flow Imaging: Current Status to Future Clinical Applications. *Current Cardiology Reports 16*, 5 (2014), 481. 2

[MWB*10] MARKL M., WALLIS W., BRENDECKE S., SIMON J., FRYDRYCHOWICZ A., A. H.: Estimation of Global Aortic Pulse Wave Velocity by Flow-sensitive 4D MRI. *Journal of Magnetic Resonance Imaging 63*, 6 (2010), 1575–82. 14

[NFL86] NAYLER G. L., FIRMIN D. N., LONGMORE D. B.: Blood Flow Imaging by Cine Magnetic Resonance. *Journal of Computer Assisted Tomography 10*, 5 (1986), 715–22. 1

[NGG*15] NEUGEBAUER M., GLÖCKLER M., GOUBERGRITS L., KELM

M., KUEHNE T., HENNEMUTH A.: Interactive Virtual Stent Planning for the Treatment of Coarctation of the Aorta. *International Journal of Computer Assisted Radiology and Surgery 11*, 1 (2015), 133–44. 20

[NJF*12] NETT E. J., JOHNSON K. M., FRYDRYCHOWICZ A., DEL RIO A. M., SCHRAUBEN E., FRANÇOIS C. J., WIEBEN O.: Four-Dimensional Phase Contrast Magnetic Resonance Imaging with Accelerated Dual Velocity Encoding. *Journal of Magnetic Resonance Imaging 35*, 6 (2012), 1462–71. 3

[NNB*15] NAYAK K. S., NIELSEN J.-F., BERNSTEIN M. A., MARKL M., GATEHOUSE P. D., BOTNAR R. M., SALONER D., LORENZ C., WEN H., HU B. S., EPSTEIN F. H., OSHINSKI J. N., RAMAN S. V.: Cardiovascular Magnetic Resonance Phase Contrast Imaging. *Journal of Cardiovascular Magnetic Resonance 17*, 71 (2015), 1–26. 2, 3

[NS72] NEREM R. M., SEED W. A.: An in Vivo Study of Aortic Flow Disturbances. *Cardiovascular Research 6*, 1 (1972), 1–14. 18

[OKML95] OSHINSKI J. N., KU D. N., MUKUNDAN S. J., LOTH F. PETTIGREW R. I.: Determination of Wall Shear Stress in the Aorta With the use of MR Phase Velocity Mapping. *Journal of Magnetic Resonance Imaging 5*, 6 (1995), 640–7. 16

[OPM*96] OSHINSKI J. N., PARKS W. J., MARKOU C. P., BERGMAN H. L., LARSON B. E., KU D. N., MUKUNDAN S. J., PETTIGREW R. I.: Improved Measurement of Pressure Gradients in Aortic Coarctation by Magnetic Resonance Imaging. *Journal of the American College of Cardiology 28*, 7 (1996), 1818–26. 17

[OPR*98] OYRE S., PAASKE W. P., RINGGAARD S., KOZERKE S., ERLANDSEN M., BOESIGER P., PEDERSEN E. M.: Automatic Accurate Non-invasive Quantitation of Blood Flow, Cross-sectional Vessel Area, and Wall Shear Stress by Modelling of Magnetic Resonance Velocity Data. *European Journal of Vascular and Endovascular Surgery: The Official Journal of the European Society for Vascular Surgery 16*, 6 (1998), 517–24. 17

[ORK*98a] OYRE S., RINGGAARD S., KOZERKE S., PAASKE W. P., ERLANDSEN M., BOESIGER P., PEDERSEN E. M.: Accurate Noninvasive Quantitation of Blood Flow, Cross-sectional Lumen Vessel Area and Wall Shear Stress by Three-dimensional Paraboloid Modeling of Magnetic Resonance Imaging Velocity Data. *Journal of the American College of Cardiology 32*, 1 (1998), 128–34. 17

[ORK*98b] OYRE S., RINGGAARD S., KOZERKE S., PAASKE W. P., SCHEIDEGGER M. B., BOESIGER P., PEDERSEN E. M.: Quantitation of Circumferential Subpixel Vessel Wall Position and Wall Shear Stress by Multiple Sectored Three-dimensional Paraboloid Modeling of Velocity Encoded Cine MR. *Journal of Magnetic Resonance in Medicine 40*, 5 (1998), 645–55. 17

[OUT*15] ONG F., UECKER M., TARIQ U., HSIAO A., ALLEY M. T., VASANAWALA S. S., LUSTIG M.: Robust 4D Flow Denoising Using Divergence-free Wavelet Transform. *Journal of Magnetic Resonance Imaging 73*, 2 (2015), 828–42. 5, 6

[PB13] PREIM B., BOTHA C.: *Visual Computing for Medicine*, 2 ed. Morgan Kaufmann Publishers, 2013. 8

[PBB05] PEETERS J. M., BOS C., BAKKER C. J.: Analysis and Correction of Gradient Nonlinearity and B0 Inhomogeneity Related Scaling Errors in Twodimensional Phase Contrast Flow Measurements. *Journal of Magnetic Resonance in Medicine 53*, 1 (2005), 126–33. 4

[PDE12] PETERSSON S., DYVERFELDT P., EBBERS T.: Assessment of the Accuracy of MRI Wall Shear Stress Estimation Using Numerical Simulations. *Journal of Magnetic Resonance Imaging 36*, 1 (2012), 128–38. 20

[PH83] PAULSEN P. K., HASENKAM J. M.: Three-dimensional Visualization of Velocity Profiles in the Ascending Aorta in Dogs, Measured with a Hot-film Anemometer. *Journal of Biomechanics 16*, 3 (1983), 201–10. 1, 9

[PMVN14] POTTERS W. V., MARQUERING H. A., VANBAVEL E., NEDERVEEN A. J.: Measuring Wall Shear Stress Using Velocity-Encoded MRI. *Current Cardiovascular Imaging Reports 7*, 4 (2014), 1–12. 16, 17

[PN85] PATTANY P. M., NAYLER G. L.: High Velocity Flow Imaging by Even Echo Rephasing. In *Proceedings: International Society for Magnetic Resonance in Medicine* (London, United Kingdom, 1985), The International Society for Magnetic Resonance in Medicine, pp. 599–600. 1

[PS05] PAPAIOANNOU T. G., STEFANADIS C.: Vascular Wall Shear Stress: Basic Principles and Methods. *Hellenic Journal of Cardiology 46*, 1 (2005), 9–15. 16

[PVH*03] POST F. H., VROLIJK B., HAUSER H., LARAMEE R. S., DOLEISCH H.: The State of the Art in Flow Visualisation: Feature Extraction and Tracking. *Computer Graphics Forum 22*, 4 (2003), 775–92. 9

[PvOM*15] POTTERS W. V., VAN OOIJ P., MARQUERING H., VANBAVEL E., NEDERVEEN A. J.: Volumetric Arterial Wall Shear Stress Calculation Based on Cine Phase Contrast MRI. *Journal of Magnetic Resonance Imaging 41*, 2 (2015), 505–16. 17

[PVOVN12] POTTERS W. V., VAN OOIJ P., VANBAVEL E., NEDERVEEN A.: Vectorial Wall Shear Stress Calculations in Vessel Structures Using 4D PC-MRI. *Journal of Cardiovascular Magnetic Resonance 14*, 1 (2012), W5. 17

[PVS*09] PICCINELLI M., VENEZIANI A., STEINMAN D. A., REMUZZI A., ANTIGA L.: A Framework for Geometric Analysis of Vascular Structures: Application to Cerebral Aneurysms. *IEEE Transactions on Medical Imaging 28*, 8 (2009), 1141–55. 7

[PWSB99] PRUESSMANN K. P., WEIGER M., SCHEIDEGGER M. B., BOESIGER P.: SENSE: Sensitivity Encoding for Fast MRI. *Journal of Magnetic Resonance in Medicine 42*, 5 (1999), 952–62. 3

[PZK*03] PAPATHANASOPOULOU P., ZHAO S., KÖHLER U., ROBERTSON M. B., LONG Q., HOSKINS P., XU X. Y., MARSHALL I.: MRI Measurement of Time-resolved Wall Shear Stress Vectors in a Carotid Bifurcation Model, and Comparison With CFD Predictions. *Journal of Magnetic Resonance Imaging 17*, 2 (2003), 153–62. 17

[Ren11] RENNER J.: *Towards Subject Specific Aortic Wall Shear Stress: A Combined CFD and MRI Approach*. PhD thesis, Linköping University, Department of Management and Engineering, Applied Thermodynamics and Fluid Mechanics. Linköping University, The Institute of Technology, 2011. 20

[SAG*14] STANKOVIC Z., ALLEN B. D., GARCIA J., JARVIS K. B., MARKL M.: 4D Flow Imaging With MRI. *Journal of Cardiovascular Diagnosis and Therapy 4*, 2 (2014), 173–92. 2, 3, 4, 20

[SCG*14] SEMAAN E. M., CARR M., GÜLSÜN M. A., VAN OOIJ P., STALDER A. F., CARR J., COLLINS J., MARKL M., SPOTTISWOODE B.: Evaluation of an Optimized Post-Processing Tool for 4D Flow MRI Data Analysis in Healthy Volunteers and Patients With Aortic Stenosis, Aortic Insufficiency, and Aortic Aneurysm. In *Proceedings: International Society for Magnetic Resonance in Medicine* (Milan, Italy, 2014), The International Society for Magnetic Resonance in Medicine, p. 3948. 20

[SDW*15] SIGOVAN M., DYVERFELDT P., WRENN J., TSENG E. E., SALONER D., HOPE M. D.: Extended 3D Approach for Quantification of Abnormal Ascending Aortic Flow. *Journal of Magnetic Resonance Imaging 33*, 5 (2015), 695–700. 15

[SFH*10] STALDER A., FRYDRYCHOWICZ A., HARLOFF A., YANG Q., BOCK J., HENNIG J., LI K. C., MARKL M.: Vortex Core Detection and Visualization Using 4D Flow-Sensitive MRI. In *Proceedings: International Society for Magnetic Resonance in Medicine* (Stockholm, Sweden, 2010), The International Society for Magnetic Resonance in Medicine. 12

[SGGJ13] STALDER A. F., GÜLSÜN M. A., GREISER A., JOLLY M.-P.: Fully Automatic Visualization of 4D Flow Data. In *Proceedings: International Society for Magnetic Resonance in Medicine* (Salt Lake City, Utah, USA, 2013), The International Society for Magnetic Resonance in Medicine, p. 1434. 7

[SGSM08] SALZBRUNN T., GARTH C., SCHEUERMANN G., MEYER J.: Pathline Predicates and Unsteady Flow Structures. *The Visual Computer 24*, 12 (2008), 1039–51. 11

[SH95] SUJUDI D., HAIMES R.: *Identification of Swirling Flow in 3-D Vector Fields*. Tech. rep., Department of Aeronautics and Astronautics, MIT, Cambridge, 1995. 12

[SH15] SCHUMANN C., HENNEMUTH A.: Three-dimensional Visualization of Relative Pressure in Vascular Structures. In *Proceedings: Computer and Robot Assisted Surgery* (Bremen, Germany, 2015), p. to appear. 17

[SHFF11] SCHWENKE M., HENNEMUTH A., FISCHER B., FRIMAN O.: Blood Flow Computation in Phase-Contrast MRI by Minimal Paths in Anisotropic Media. In *Proceedings: Medical Image Computing and Computer Assisted Intervention* (Toronto, Canada, 2011), Springer, pp. 436–43. 20

[SHG*06] SALFITY M. F., HUNTLEY J. M., GRAVES M. J., MARKLUND O., CUSACK R., BEAUREGARD D. A.: Extending the Dynamic Range of Phase Contrast Magnetic Resonance Velocity Imaging Using Advanced Higher-Dimensional Phase Unwrapping Algorithms. *Journal of The Royal Society Interface 3*, 8 (2006), 415–27. 4

[SLB*15] SANTELLI C., LOECHER M., BUSCH J., WIEBEN O., SCHAEFFTER T., KOZERKE S.: Accelerating 4D Flow MRI by Exploiting Vector Field Divergence Regularization. *Journal of Magnetic Resonance in Medicine 75*, 1 (2015), 115–25. 6

[SLWL09] SRICHAI M. B., LIM R. P., WONG S., LEE V. S.: Cardiovascular Applications of Phase-contrast MRI. *American Journal of Roentgenology 192*, 3 (2009), 662–75. 2

[SMBB*13] SCHULZ-MENGER J., BLUEMKE D. A., BREMERICH J., FLAMM S. D., FOGEL M. A., FRIEDRICH M. G., KIM R. J., VON KNOBELSDORFF-BRENKENHOFF F., KRAMER C. M., PENNELL D. J., PLEIN S., NAGEL E.: Standardized Image Interpretation and Post Processing in Cardiovascular Magnetic Resonance: Society for Cardiovascular Magnetic Resonance (SCMR) Board of Trustees Task Force on Standardized Post Processing. *Journal of Cardiovascular Magnetic Resonance 15*, 35 (2013). 13

[SME*14] SCHNELL S., MARKL M., ENTEZARI P., MAHADEWIA R. J., SEMAAN E. M., STANKOVIC Z., COLLINS J., CARR J., JUNG B.: k-t GRAPPA Accelerated Four-Dimensional Flow MRI in the Aorta: Effect on Scan Time, Image Quality, and Quantification of Flow and Wall Shear Stress. *Journal of Magnetic Resonance in Medicine 72*, 2 (2014), 522–33. 3

[SNPG95] SONG S. M.-H., NAPEL S., PELC N. J., GLOVER G. H.: Phase Unwrapping of MR Phase Images Using Poisson Equation. *IEEE Transactions on Image Processing 4*, 5 (1995), 667–76. 4

[SPH04] SOLEM J. E., PERSSON M., HEYDEN A.: Velocity Based Segmentation in Phase Contrast MRI Images. In *Proceedings: Medical Image Computing and Computer Assisted Intervention* (St. Malo, France, 2004), Springer, pp. 459–66. 6

[SPK*12] SENGUPTA P. P., PEDRIZZETTI G., KILNER P. J., KHERADVAR

A., EBBERS T., TONTI G., FRASER A. G., NARULA J.: Emerging Trends in CV Flow Visualization. *JACC: Cardiovascular Imaging 5*, 3 (2012), 305–16. 2

[SRF*08] STALDER A. F., RUSSE M. F., FRYDRYCHOWICZ A., BOCK J., HENNIG J., MARKL M.: Quantitative 2D and 3D Phase Contrast MRI: Optimized Analysis of Blood Flow and Vessel Wall Parameters. *Journal of Magnetic Resonance in Medicine 60*, 5 (2008), 1218–31. 17

[SS76] STEIN P. D., SABBAH H. N.: Turbulent Blood Flow in the Ascending Aorta of Humans With Normal and Diseased Aortic Valves. *Circulation Research 39*, 1 (1976), 58–65. 18

[SS07] SIEVERS H. H., SCHMIDTKE C.: A Classification System for the Bicuspid Aortic Valve from 304 Surgical Specimens. *The Journal of Thoracic and Cardiovascular Surgery 133*, 5 (2007), 1226–33. 2

[SSG*13] SPOTTISWOODE B., STALDER A. F., GÜLSÜN M. A., CAMPIONE K. F., CARR M., WASIELEWSKI M., MARKL M.: Fast semi-automated analysis of pulse wave velocity in the thoracic aorta using high temporal resolution 4D flow MRI. *Journal of Cardiovascular Magnetic Resonance 15*, Suppl 1 (2013), P87. 15

[STH*09] SHI K., THEISEL H., HAUSER H., WEINKAUF T., MATKOVIC K., HEGE H.-C., SEIDEL H.-P.: Path Line Attributes – an Information Visualization Approach to Analyzing the Dynamic Behavior of 3D Time-Dependent Flow Fields. In *Topology-based Methods in Visualization II* (Grimma, Germany, 2009), Springer, pp. 75–88. 11

[SUV*15] SOTELO J., URBINA J., VALVERDE I., TEJOS C., IRARRÀZAVAL P., HURTADO D. E., URIBE S.: Quantification of Wall Shear Stress Using a Finite-element Method in Multidimensional Phase-contrast MR Data of the Thoracic Aorta. *Journal of Biomechanics 48*, 10 (2015), 1817–27. 17

[SW71] SEED W. A., WOOD N. B.: Velocity Patterns in the Aorta. *Cardiovascular Research 5*, 3 (1971), 319–30. 1

[SZ03] SCHOFIELD M. A., ZHU Y.: Fast Phase Unwrapping Algorithm for Interferometric Applications. *Optics Letters 28*, 14 (2003), 1194–6. 4

[Tag14] TAGLIASACCHI A.: *Skeletal Representations and Applications*. Tech. rep., School of Computing Science, Simon Fraser University, 2014. 7

[TBW01] TSAO J., BEHNIA B., WEBB A. G.: Unifying Linear Prior-Information-Driven Methods for Accelerated Image Acquisition. *Journal of Magnetic Resonance in Medicine 46*, 4 (2001), 652–60. 3

[TDGSU11] TAFTI P. D., DELGADO-GONZALO R., STALDER A. F., UNSER M.: Variational Enhancement and Denoising of Flow Field Images. In *Proceedings: IEEE International Symposium on Biomedical Imaging* (Chicago, Illinois, USA, 2011), IEEE Computer Society, pp. 1061–4. 5

[TKC*12] TÖGER J., KANSKI M., CARLSSON M., KOVÁCS S. J., SÖDERLIND G., ARHEDEN H., HEIBERG E.: Vortex Ring Formation in the Left Ventricle of the Heart: Analysis by 4D Flow MRI and Lagrangian Coherent Structures. *Annals of Biomedical Engineering 40*, 12 (2012), 2652–62. 19

[TLAS00] TYSZKA J. M., LAIDLAW D. H., ASA J. W., SILVERMAN J. M.: Three-dimensional, Time-resolved (4D) Relative Pressure Mapping Using Magnetic Resonance Imaging. *Journal of Magnetic Resonance Imaging 12*, 2 (2000), 321–9. 18

[TU11] TAFTI P. D., UNSER M.: On Regularized Reconstruction of Vector Fields. *IEEE Transactions on Image Processing 20*, 11 (2011), 3163–78. 5

[UFK*87] UNDERWOOD S. R., FIRMIN D. N., KLIPSTEIN R. H., REES R. S. O., LONGMORE D. B.: Magnetic Resonance Velocity Mapping: Clinical Application of a New Technique. *British Heart Journal 57*, 5 (1987), 404–12. 1

[UHT*15] UNTENBERGER M., HÜLLEBRAND M., TAUTZ L., JOSEPH A. A., VOIT D., MERBOLDT K. D., FRAHM J.: Spatiotemporal Phase Unwrapping for Real-time Phase-contrast Flow MRI. *Journal of Magnetic Resonance in Medicine 74*, 4 (2015), 964–70. 4

[Ven10] VENKATARAMAN S.: 4D Visualization of Cardiac Flow, 2010. NVIDIA GPU Technology Conference Talk. 9

[vOPC*15] VAN OOIJ P., POTTERS W. V., COLLINS J., CARR M., CARR J., MALAISRIE S. C., FEDAK P. W., MCCARTHY P. M., MARKL M., BARKER A. J.: Characterization of Abnormal Wall Shear Stress Using 4D Flow MRI in Human Bicuspid Aortopathy. *Annals of Biomedical Engineering 43*, 6 (2015), 1385–97. 2

[VOPG*13] VAN OOIJ P., POTTERS W. V., GUÉDON A., SCHNEIDERS J. J., MARQUERING H. A., MAJOIE C. B., VANBAVEL E., NEDERVEEN A. J.: Wall Shear Stress Estimated with Phase Contrast MRI in an In Vitro and In Vivo Intracranial Aneurysm. *Journal of Magnetic Resonance Imaging 38*, 4 (2013), 876–84. 17

[vOPP*15] VAN OOIJ P., POWELL A. L., POTTERS W. V., CARR J. C., MARKL M., BARKER A. J.: Reproducibility and Interobserver Variability of Systolic Blood Flow Velocity and 3D Wall Shear Stress Derived from 4D Flow MRI in the Healthy Aorta. *Journal of Magnetic Resonance Imaging 43*, 1 (2015), 236–48. 3

[VPBB*10] VAN PELT R. F. P., BESCÓS J. O., BREEUWER M., CLOUGH R. E., GRÖLLER M. E., TER HAAR ROMENY B. M., VILANOVA A.: Exploration of 4D MRI Blood Flow Using Stylistic Visualization. *IEEE Transactions on Visualization and Computer Graphics 16*, 6 (2010), 1339–47. 1, 6, 8, 13, 20

[VPBB*11] VAN PELT R. F. P., BESCÓS J. O., BREEUWER M., CLOUGH R. E., GRÖLLER M. E., TER HAAR ROMENY B. M., VILANOVA A.: Interactive Virtual Probing of 4D MRI Blood-Flow. *IEEE Transactions on Visualization and Computer Graphics 17*, 12 (2011), 2153–62. 10, 11

[VPFCV14] VAN PELT R. F. P., FUSTER A., CLAASSEN G. G. H., VILANOVA A.: Characterization of Blood-Flow Patterns from Phase-Contrast MRI Velocity Fields. In *Eurographics Conference on Visualization (EuroVis) - Short Papers* (Swansea, UK, 2014), The Eurographics Association. 13

[VPJtHRV12] VAN PELT R. F. P., JACOBS S. S. A. M., TER HAAR ROMENY B. M., VILANOVA A.: Visualization of 4D Blood-Flow Fields by Spatiotemporal Hierarchical Clustering. *Computer Graphics Forum 31*, 3 (2012), 1065–74. 11

[VPNtHRV12] VAN PELT R. F. P., NGUYEN H., TER HAAR ROMENY B. M., VILANOVA A.: Automated Segmentation of Blood-Flow Regions in Large Thoracic Arteries Using 3D-Cine PC-MRI Measurements. *International Journal for Computer Assisted Radiology and Surgery 7*, 2 (2012), 217–24. 7

[VPV13] VAN PELT R. F. P., VILANOVA A.: Understanding Blood-Flow Dynamics: New Challenges for Visualization. *Computer 46*, 12 (2013), 60–7. 20

[VPvP*14] VILANOVA A., PREIM B., VAN PELT R. F. P., GASTEIGER R., NEUGEBAUER M., WISCHGOLL T.: *Visual Exploration of Simulated and Measured Blood Flow*. Springer-Verlag London, 2014, ch. 25, pp. 305–20. 11

[vSCG*15] VON SPICZAK J., CRELIER G., GIESE D., KOZERKE S., MAINTZ D., BUNCK A. C.: Quantitative Analysis of Vortical Blood Flow in the Thoracic Aorta Using 4D Phase Contrast MRI. *PLoS ONE 10*, 9 (2015). 12, 19

[VTC*15] VOLONGHI P., TRESOLDI D., CADIOLI M., USUELLI A. M., PONZINI R., MORBIDUCCI U., ESPOSITO A., RIZZO G.: Automatic Extraction of Three-dimensional Thoracic Aorta Geometric Model from Phase Contrast MRI for Morphometric and Hemodynamic Characterization. *Journal of Magnetic Resonance in Medicine 75*, 2 (2015), 873–82. 7

[VZ03] VOLKOV V. V., ZHU Y.: Deterministic Phase Unwrapping in the Presence of Noise. *Optics Letters 28*, 22 (2003), 2156–8. 4

[WCS*93] WALKER P. G., CRANNEY G. B., SCHEIDEGGER M. B., WASELESKI G., POHOST G. M., YOGANATHAN A. P.: Semiautomated Method for Noise Reduction and Background Phase Error Correction in MR Phase Velocity Data. *Journal of Magnetic Resonance Imaging 3*, 3 (1993), 521–30. 4, 5, 7

[WEF*99] WIGSTRÖM L., EBBERS T., FYRENIUS A., KARLSSON M., ENGVALL J., WRANNE B., BOLGER A. F.: Particle Trace Visualization of Intracardiac Flow Using Time-Resolved 3D Phase Contrast MRI. *Journal of Magnetic Resonance in Medicine 41*, 4 (1999), 793–9. 10

[WGW13] WENTLAND A. L., GRIST T. M., WIEBEN O.: Repeatability and Internal Consistency of Abdominal 2D and 4D Phase Contrast MR Flow Measurements. *Academic Radiology 20*, 6 (2013), 699–704. 3

[WGW14] WENTLAND A. L., GRIST T. M., WIEBEN O.: Review of MRI-based Measurements of Pulse Wave Velocity: a Biomarker of Arterial Stiffness. *Journal of Cardiovascular Diagnosis and Therapy 4*, 2 (2014), 193–296. 14, 15

[WKS*09] WÖHRLE J., KOCHS M., SPIESS J., NUSSER T., HOMBACH V., MERKLE N.: Impact of Percutaneous Device Implantation for Closure of Patent Foramen Ovale on Valve Insufficiencies. *Circulation 119*, 23 (2009), 3002–8. 14

[WKW*09] WONG K. K. L., KELSO R. M., WORTHLEY S. G., SANDERS P., MAZUMDAR J., D. A.: Cardiac Flow Analysis Applied to Phase Contrast Magnetic Resonance Imaging of the Heart. *Annals of Biomedical Engineering 37*, 8 (2009), 1495–515. 19

[WSN10] WESTERHOF N., STERGIOPULOS N., NOBLE M. I. M.: *Snapshots of Hemodynamics: An Aid for Clinical Research and Graduate Education*. Springer, 2010. 16

[WSW96] WIGSTRÖM L., SJÖQVIST L., WRANNE B.: Temporally Resolved 3D Phase-Contrast Imaging. *Journal of Magnetic Resonance Imaging 36*, 5 (1996), 800–3. 2

[WTK*10] WONG K. K. L., TU J., KELSO R. M., WORTHLEY S. G., P. S., MAZUMDAR J., D. A.: Cardiac Flow Component Analysis. *Medical Engineering & Physics 32*, 2 (2010), 174–88. 19

[WWF*13] WENTLAND A. L., WIEBEN O., FRANÇOIS C. J., BONCYK C., MUNOZ DEL RIO A., JOHNSON K. M., GRIST T. M., FRYDRYCHOWICZ A.: Aortic Pulse Wave Velocity Measurements With Undersampled 4D Flow-Sensitive MRI: Comparison With 2D and Algorithm Determination. *Journal of Magnetic Resonance Imaging 37*, 4 (2013), 853–9. 15

[Xia95] XIANG Q.-S.: Temporal Phase Unwrapping for CINE Velocity Imaging. *Journal of Magnetic Resonance Imaging 5*, 5 (1995), 529–34. 4

[YBK*96] YANG G. Z., BURGER P., KILNER P. J., KARWATOWSKI S. P., FIRMIN D. N.: Dynamic Range Extension of Cine Velocity Measurements Using Motion-Registered Spatiotemporal Phase Unwrapping. *Journal of Magnetic Resonance Imaging 6*, 3 (1996), 495–502. 4

[YBKM91] YANG G. Z., BURGER P., KILNER P. J., MOHIADDIN R. H.: In Vivo Blood Flow Visualization with Magnetic Resonance Imaging. In *Proceedings: IEEE Conference on Visualization (Vis)* (San Diego, California, USA, 1991), IEEE Computer Society, pp. 202–9. 10

[YHGT10] YANG J. C., HENSLEY J., GRÜN H., THIBIEROZ N.: Real-time Concurrent Linked List Construction on the GPU. *Computer Graph-*

ics Forum (2010), 1297–304. 10

[YKW*96] YANG G. Z., KILNER P. J., WOOD N. B., UNDERWOOD S. R., FIRMIN D. N.: Computation of Flow Pressure Fields From Magnetic Resonance Velocity Mapping. *Journal of Magnetic Resonance in Medicine 36*, 4 (1996), 520–6. 17

[YPW*06] YU H. Y., PENG H. H., WANG J. L., WEN C. Y., TSENG W. Y.: Quantification of the Pulse Wave Velocity of the Descending Aorta Using Axial Velocity Profiles from Phase-contrast Magnetic Resonance Imaging. *Journal of Magnetic Resonance in Medicine 56*, 4 (2006), 876–83. 15

[ZSH96] ZÖCKLER M., STALLING D., HEGE H.-C.: Interactive Visualization of 3D-vector Fields Using Illuminated Stream Lines. In *Proceedings: IEEE Conference on Visualization (Vis)* (San Francisco, California, USA, 1996), IEEE Computer Society, pp. 107–13. 10